PNAS
www.pnas.org

Supplementary Information for:

The internal structure and geodynamics of Mars inferred from a 4.2 Gyr zircon record

Maria M. Costa, Ninna K. Jensen, Laura C. Bouvier, James N. Connelly, Takashi Mikouchi, Matthew S.A. Horstwood, Jussi-Petteri Suuronen. Frederic Moynier, Zhengbin Deng, Arnaud Agranier, Laure A. J. Martin, Tim E. Johnson, Alexander A. Nemchin and Martin Bizzarro

Martin Bizzarro
Email: bizzarro@sund.ku.dk

This PDF file includes:

Material and methods
Supplementary text
Figures S1 to S16
Tables S1 to S10
Legend for Dataset S1
SI References

Other supplementary materials for this manuscript include the following:

Dataset S1

www.pnas.org/cgi/doi/10.1073/pnas.2016326117

Material and methods

Sample preparation and zircon extraction. Around 15g of the NWA 7533 meteorite were gently crushed using an agate mortar and pestle to a granularity inferior to 150 μm. Subsequently, the sample was subjected to magnetic separation using a Frantz isodynamic separator at progressively higher magnetic fields until the most magnetic mineral phases were removed and the resultant non-magnetic fraction further purified with heavy liquids. Due to the absence of crystals with the characteristic zircon habits and also the reduced size of many of the grains, it was not possible to identify the crystals by simple observation of the sample under a microscope. As such, the dense, non-magnetic mineral separate was spread on glass slides and scanned multiple times in a micro x-ray fluorescence Bruker M4 Tornado, in order to isolate the crystals typified by a zirconium peak in high sensitivity scans. Around 100 grains, mostly zircon but also some rare baddeleyite, were identified and isolated. Given the delicate character of the sample and the reduced dimensions of most of the crystals extracted from it, to minimise handling and the consequent risk of losing them, no methods of abrasion were applied to the crystals presented in this study. An aliquot of approximately 10 mg of clast C27 was selected for bulk crushing to a particle size <200 μm. The clast fragment was submerged in Milli-Q water in an agate mortar and tapped gently with a pestle. To avoid fragmenting already-liberated crystals, the clast material was continually passed through a 200-μm mesh sieving paper into a large Pyrex beaker. After allowing all crystals to settle. the Milli-Q water was carefully decanted from the beaker, and the <200 μm-sized clast material was transferred to a petri dish using ethanol. Due to the small sample size, the crushed material was not processed through a magnetic separator nor subjected to heavy liquids separation. The crushed material was spread on a glass slide and scanned multiple times in a micro X-ray fluorescence Bruker M4 Tornado in order to isolate the crystals typified by a zirconium peak in high sensitivity scans. A total of 21 zircons ranging in size from 15 to 70 μm were identified, from which the four largest were selected for isotopic investigation.

Description of zircons. The zircons extracted from the crushed aliquot of the NWA 7533 meteorite breccia differ in size, shape and degree of evidence for radiation damage. They range from about 20 to 110 μm in size although most of the grains were between 20 and 40 μm. Crystals with sizes below 20 μm were also recovered in the separation process but they were not used in this study mostly due to the difficulty in handling these crystals. Based on the observed crystal shapes and/or degree of metamictization, four different zircon populations were defined. The first one is characterized by light brown, anhedral grains, with a sugary granulated texture making these very delicate to handle as they easily disintegrate when touched (Fig. S5). The appearance of this population is similar to that of strongly metamict crystals and, as such, they were not used for this study. A second population is characterized by rounded crystals, colourless or pale to yellow in colour. Most of these crystals appear crystalline under microscopic inspection except for a couple grains of strong yellow colour, which look cloudy. Fractures are uncommon in this population. One zircon from this population, dubbed DT-1, was recognised to host a number of inclusions. The DT-1 zircon is an 83×73×50 μm, colorless and glassy crystal, characterized by a subhedral habit given that only some faces of its original flat prismatic shape are preserved due to the general rounded aspect of the crystal. To preserve the inclusions for future work, the DT-1 zircon was strategically polished and only investigated using *in situ* techniques. In detail, the U-Pb and Hf isotopes were investigated for this zircon using secondary ionization mass spectrometry (SIMS) and laser-ablation multiple collection plasma source mass spectrometry (LA-MC-ICPMS), respectively. The most abundant type of crystals recovered from this meteorite are anhedral and colourless grains with some exhibiting fractures and inclusions. Two types of inclusions were observed, a dark, presumed oxide mineral phase that could be ilmenite and a colourless mineral or fluid inclusion that was not positively identified. Despite most of these crystals being completely transparent, there are a few cloudy grains, especially noticeable when observed dry. This population shows the largest variation in grain sizes and yielded most of the largest crystals analysed in this study. Finally, the last zircon population observed is extremely rare and composed just by a few grains with euhedral to subhedral habits that preserve at least two original faces. Most of the crystals are completely glassy whereas others exhibit less clear domains. Some grains have fractures but inclusions are scarce and they range from colourless to pale brown in colour. Grains from all the populations, except the granulated ones, were considered for dissolution and analysis. All the

available anhedral, subhedral and euhedral grains with sizes above 40 µm and no visible inclusions were dissolved. Other than those, the clearest crystals from sizes from 20-40 µm were also dissolved, as well as some of the round, yellow population. Only minor amounts of baddeleyite crystals were recovered from the separation process. The crystals are mainly subhedral, with a tendency to show the elongated, tabular shape typical for baddeleyite, although anhedral grains were also found. They range in size from about 15 µm to 70 µm long and exhibit colours ranging from pale brown to colourless.

Solution mode U-Pb geochronology of zircons. Before complete dissolution, all zircon grains were cleaned in Pyrex beakers in an ultrasonic bath with alternating steps of warm 3.5 M HNO_3, H_2O and acetone (1). Assuming that each grain may represent a different age, they were processed as single-grains. The crystals were then dissolved in separate PFE Teflon capsules in an HF-HNO_3 (3:1) mixture, together with the mixed ^{202}Pb-^{205}Pb-^{233}U -^{235}U EARTHTIME U-Pb tracer (2), for four days at 210°C. After dissolution, the samples were evaporated to dryness and redissolved in 3.1M HCl overnight. Uranium and lead were separated and purified from the matrix elements by anion chromatography using 50 ml Teflon columns (3,4) and dried down with 8 µl of 0.1 M H_3PO_4. They were loaded with silica gel (5) on previously outgassed zone-refined rhenium filaments. The Pb and U isotopic ratios of the sample-tracer mixture were measured using a Thermo-Fisher thermal ionization mass spectrometer, where each isotope was sequentially counted in a single axial ion counting system with Pb as Pb^+, and U as UO_2^+. The data was reduced offline and instrumental mass fractionation was accounted for by a linear mass dependent fractionation law based on the $^{202}Pb/^{205}Pb$ ratio of the tracer. All the common Pb was removed as laboratory blank. Instrumental mass-dependent fractionation of U was accounted for using the $^{233}U/^{235}U$ ratio of the tracer, which included a correction for the isobaric interference of $^{233}U^{16}O^{18}O$ on the $^{235}U^{16}O_2$ peak at mass 267. The ^{238}U and ^{235}U decay constants of Jaffey *et al*. (6) and a $^{238}U/^{235}U$ ratio of 137.88 (7) were used for age calculation. All age uncertainties are quoted at the 95% confidence level.

Solution mode Lu-Hf systematics of zircons. The Hf isotope composition and Lu/Hf ratios of individual zircons were determined from the same sample digestion used for U-Pb age determination. Following collection of the washes from the U-Pb purification, approximately 5% of the solution was aliquoted for Lu/Hf ratio determination. The Hf was purified from the remaining solution by a two-step procedure using TEVA-spec and TODGA resins (Eichrom Industries) based on protocols outlined in Bizzarro *et al.* (8) and in Connelly *et al.* (9). Zr was quantitatively separated from Hf, Ti and REE using 100-150 µm TEVA-spec resin in 120 µL column. The HFSE-REE fractions were loaded in 0.6 mL of 10.5M HCl and a Hf+Ti+REE cut was successively collected with 3.6mL of 10.5M HCl and 4.2 mL of 9.5M HCl. Zr was recovered with 3.0 mL of 6M HCl. Hf was purified from Ti and REE using 50-100 µm TODGA resin in 200 µL columns. The Hf+Ti+REE fractions were loaded in 0.85mL of 3.5M HNO_3-0.06M boric acid and the Ti was eluted by adding 3.5 mL of 3.5M HNO_3 while Hf and REE remained on the column. Hf was subsequently collected with 6 mL of 1M HNO_3-0.35M HF. This method returns Hf yields greater than 95% in Hf cuts with Zr/Hf ratios below 1. Hf isotope ratios were measured on the *Pandora* Thermo-Fisher Neptune Plus Multi-Collector Inductively Coupled Mass Spectrometer (MC-ICPMS) at the Centre for Star and Planet Formation, University of Copenhagen, using a sample-standard bracketing technique. Samples were aspirated into the plasma source in 2% HNO_3-0.1M HF solution via a Cetac Aridus II desolvating nebulizer using Ar and N sweep gases with an uptake rate of ~100 µl/min. Typical sensitivity at this uptake rate was 1800V per ppm for Hf. Hafnium isotopic data were acquired in static mode using eight Faraday collectors allowing for simultaneous measurement of ^{176}Hf, ^{177}Hf, ^{178}Hf, ^{179}Hf and ^{180}Hf as well as monitoring potential isobaric interferences (^{176}Yb on ^{176}Hf, ^{176}Lu on ^{176}Hf and ^{180}W on ^{180}Hf) using ^{175}Lu, ^{171}Yb and ^{182}W. Faraday detectors used to collect Hf isotopes and ^{182}W were connected to amplifiers with 10^{11} Ohm feedback resistors whereas ^{175}Lu and ^{171}Yb were measured on Faraday detectors connected to amplifiers with 10^{13} Ohm feedback resistors. Sample analyses were interspersed with analyses of the JMC-475 standard as follows: JMC-475 (1), JMC-475 (2), sample-1, JMC-475 (3), JMC-475 (4). Samples and standards were analyzed with a signal intensity of at least 0.5V on mass ^{177}Hf and ensuring that the signal intensity of the sample and standard were matched to within 5 %. Samples were analyzed once and the total amount of Hf consumed per analysis was typically 0.5-5 ng for NWA 7533 zircons. Total procedural

blanks were <10 pg for Hf, an amount that is negligible for all samples considering the amount of Hf available for analysis. All data reduction was conducted off-line using the Iolite data reduction software (10) that runs within Igor Pro. Background intensities were interpolated using a smoothed cubic spline, as were changes in mass bias with time. Hf isotope data were corrected for mass bias using the exponential mass fractionation law adopting $^{179}Hf/^{177}Hf = 0.7325$. The sample $^{176}Hf/^{177}Hf$, $^{178}Hf/^{177}Hf$, $^{180}Hf/^{177}Hf$ ratios were normalised to the JMC-475 reference values of 0.282160, 1.46717 and 1.88667, respectively. Contribution from interfering species were typically less than 50 and 10 ppm on $^{176}Hf/^{177}Hf$ from Yb and Lu, respectively, and 100 ppm on $^{180}Hf/^{177}Hf$ from W. Doping experiments with Yb, Lu and W interference levels at least 10 times greater than typically observed in our sample demonstrate that our interference correction is accurate. The accuracy and external reproducibility of our method was assessed by repeat analyses of the 91500 zircon reference standard (11). In an earlier report (1), we tested the accuracy of our Hf isotope data by analyzing seven aliquots of the same sample dissolution each containing approximately 5 ng of Hf, which yielded average values for the $^{176}Hf/^{177}Hf$, $^{178}Hf/^{177}Hf$, $^{180}Hf/^{177}Hf$ ratios of the 91500 standard aliquots of 0.282311±0.000006, 1.46718±0.00002 and 1.88669±0.00006, respectively. As the amounts of Hf recovered from the zircons in the current study were, in some cases, less than 5 ng, we analysed nine aliquots of the same sample dissolution of the 91500 standard each containing approximately 1 ng of Hf and individually processed through our U-Pb and Hf purification scheme. The average values obtained for the $^{176}Hf/^{177}Hf$, $^{178}Hf/^{177}Hf$, $^{180}Hf/^{177}Hf$ ratios of the 91500 standard aliquots were 0.282309±0.000018, 1.46718±0.000032 and 1.88669±0.00010, where the uncertainty represents the external reproducibility (2SD) (Table S4). The data we obtained for the 91500 zircon reference standard are identical to published values (12). The Lu/Hf ratios were determined by the same MC-ICPMS as used for the Hf isotopic measurements using gravimetrically prepared mixed Lu-Hf standard solutions. In detail, the ~5% aliquot reserved for Lu/Hf ratio determination was evaporated and re-dissolved in 2% HNO_3-0.1M HF prior to analysis. Samples were aspirated into the plasma source via a Cetac Aridus II desolvating nebulizer using Ar and N sweep gases with an uptake rate of ~100 µL/min. The ^{175}Lu beam was collected on the axial secondary electron multiplier (SEM) whereas the ^{177}Hf was collected on the H2 faraday detector connected to an amplifier with a 10^{11} Ohm feedback resistor. Sample analyses were interspaced by analyses of the calibrated Lu-Hf standard solution as follows: Lu-Hf standard (1), Lu-Hf standard (2), sample-1, Lu-Hf standard (3), Lu-Hf standard (4). Samples and standard were analyzed with an intensity at least ~0.01 V on mass ^{177}Hf and ~25.000 cps on mass ^{175}Lu, ensuring that the signal intensity of the sample and standard were matched to within ~5%. Total procedural blanks were <5 fg for Lu and negligible for all samples considering the amount of Lu available for analysis. The Lu-Hf standard solution was prepared gravimetrically to match the typical Lu/Hf ratio of zircon and is accurate to 2%. The external reproducibility of our approach was estimated by repeated analysis of the 91500 zircon standard. Analysis of 5 individual aliquots of a single dissolution of the 91500 zircon standard yielded a $^{176}Lu/^{177}Hf$ ratio of 0.00031430±0.0000011 (2SD). which corresponds to an external reproducibility of 0.4% for the Lu/Hf ratio. Potential fractionation of the Lu/Hf ratio induced by U-Pb purification was evaluated by measuring the Lu/Hf ratios of aliquots of the 91500 zircon standard before and after U-Pb purification. Our tests demonstrate that potential fractionation of the Lu/Hf during U-Pb purification is less than 0.4%. Combined with the uncertainty of the Lu-Hf standard solution, the external reproducibility of 0.4% and the potential fractionation of 0.4%, we infer an accuracy of 2.1% for our Lu/Hf ratio measurements. The initial Hf isotope composition of the zircons/baddeleyite crystals was calculated with their corresponding $^{207}Pb/^{206}Pb$ ages (or $^{238}U/^{206}Pb$ ages for grains younger than 800 Ma) using a $\lambda^{176}Lu$ value of $1.867±0.008×10^{-11}$ $year^{-1}$ (13) and Chondritic Uniform Reservoir (CHUR) parameters of (14). The uncertainties associated with the measured Hf isotope composition, age, and that of the Lu/Hf ratio measurements have been propagated in the final uncertainty quoted for the initial Hf isotope compositions.

Rare Earth element concentration of NWA 7533 zircons. We conducted REEs concentration determination for some of the larger zircons, where sufficient material was available. Dilute sample aliquots of the individual zircons were analyzed using the high-resolution inductively coupled plasma mass spectrometer Thermo Scientific Element XR at Laboratoire Géosciences Océan (Université de Brest) for the following isotopes: ^{139}La, ^{140}Ce, ^{141}Pr, ^{146}Nd, ^{147}Sm, ^{151}Eu, ^{157}Gd, ^{159}Tb,

^{163}Dy, ^{165}Ho, ^{167}Er, ^{169}Tm, ^{174}Yb, ^{175}Lu and ^{91}Zr. All elements were calibrated using standard solutions (0.1, 1, 10, and 100 ppb), and their count rates were blank-corrected. Indium (^{115}In) was used as an internal standard to correct all data for instrumental mass bias during the analyses. Results on the mixed standards demonstrated external reproducibility better than 5% for concentrations higher than 50 ppb, and ranging from 5 to 20% for lower concentrations. As the small zircon sizes rendered mass determination untenable, it was not possible to directly obtained absolute concentration data. Therefore, all trace element data were normalized to Zr, assuming that the Zr content of the zircon is 49%. Using this approach, three aliquots of the 91500 zircon standard yielded chondrite-normalized REE patterns that compare favourably with literature data (15).

Major and trace element composition of basaltic clast C27. A polished section of clast C27 was characterized for petrology by scanning electron microprobe (SEM) at the Institut de Physique du Globe de Paris (IPGP). For a well-polished and flat sample surface, the SEM can provide major element compositions for the sample that are reliable in a sub weight percent uncertainty, as corroborated by results we obtained from basaltic glass BHVO-2G. Following SEM characterization, a 1.5 mg aliquot of clast C27 was digested using HF-HNO_3 acid mixtures. The major and trace element composition of the clast was analyzed using the Agilent 7900 quadrupole inductively coupled plasma (Q-ICP-MS) at IPGP. Helium gas (5 mL/min) was used to remove molecular interferences in a collision-reaction interface. Scandium and indium solutions were admixed to the sample solutions and were used as internal standards to correct for matrix effects and signal drift. Standard solutions with concentrations spanning those of samples were prepared from mixing certified standards and were used to generate calibration lines between count measurements and concentrations. To overcome yield effects, MgO contents from SEM mapping were used as internal normalization standard to return the Q-ICP-MS data into concentrations. The SiO_2 contents from SEM were also adopted, as silicon of samples was lost as SiF_4 during HF digestion. Repeated analyses of the BHVO-2 rock standard indicate that the data are accurate to 5%.

Electron microprobe analyses of mineralogical phases from clast C27. Backscattered electron imaging, X-ray element mapping and quantitative mineral analyses were conducted for clast C27 by field-emission (FE) electron probe microanalysis (EPMA) using the FE-EPMA JEOL JXA-8530F at the Department of Earth and Planetary Science, University of Tokyo. Element mapping was performed by wavelength dispersive spectrometry (WDS) at an accelerating voltage of 15 kV, 80 nA beam current, 6 μm beam diameter and 15 ms dwell time. Quantitative mineral analyses were conducted by WDS at an electron beam voltage and current of 15 kV and 12 nA, respectively. Silicates and Fe-oxides were analyzed with a probe diameter of 1 μm and 10 s counting times at peak wavelengths. Phosphate analyses were conducted with a probe diameter of 5 μm and 10 s counting times at peak wavelengths, except for Y, La, Ce and Nd, which were measured for 30 s at peak wavelengths. Background intensities were counted on both sides of the peak for half the peak measurement time. Peak counts were reduced to oxide weight percent using a ZAF correction method. To ensure the exclusion of phosphate analyses that overlap silicate phases, phosphate data with SiO_2>1 wt% were discarded. Spinel and ilmenite total FeO contents from EPMA were recalculated into divalent and trivalent Fe oxides (16).

In situ U-Pb geochronology of the DT-1 zircon. U-Pb zircon analyses were made using a CAMECA 1280 ion microprobe equipped with a high-brightness Oregon Physics Hyperion-II RF-plasma oxygen ion source and housed by the Centre for Microscopy, Characterisation and Analysis at the University of Western Australia. Prior to analysis, the sample mount was cleaned, dried, and coated with ~30nm of gold. The analytical procedure broadly followed that described elsewhere (17). The mass filtered $^{16}O^{2-}$ primary ion beam of about 5 nA focussed in Gaussian mode was rastered over a 5x5 μm area during the analysis. Before each analysis, an area of 15 μm was pre-sputtered for 70 seconds to remove gold coating and limit effects of surface contamination around the analytical spots. This procedure was followed by automatic centring of the secondary ion beam in the 3000 μm field aperture and optimisation of mass calibration and secondary ion beam energy distribution, performed automatically for each run using the $^{90}Zr_2{}^{16}O^+$ species at a nominal mass of

196. The mass spectrometer was operated with a mass resolution of 5500 (M/ΔM), sufficient to separate Pb peaks from molecular interferences. The sample chamber was flooded with oxygen during the session to enhance Pb ion production (18). The secondary ions of $^{90}Zr_2{}^{16}O$, $^{92}Zr_2{}^{16}O$, background, $^{94}Zr_2{}^{16}O$, ^{204}Pb, ^{206}Pb, ^{207}Pb, ^{208}Pb, $^{177}Hf^{16}O_2$, ^{232}Th, ^{238}U, $^{232}Th^{16}O$, $^{238}U^{16}O$ and $^{238}U^{16}O_2$ were measured utilising a "peak hopping" routine over 15 cycles and using a single low-noise ion counting electron multiplier. Data reduction was performed using a software developed at the NordSIM facility (Swedish Museum of Natural History). Calibration of Pb/U ratios used an empirical power law relationship between ^{206}Pb /^{238}U and $^{238}U^{16}O$/^{238}U ratios corrected against 1065 Ma zircon crystal 91500 (19). Common Pb corrections, applied to the data, used a modern-day average terrestrial Pb composition (20), assuming that most of this Pb is a result of terrestrial (surface) contamination remaining after pre-sputtering. Age calculations were made using the Excel add-in Isoplot with the decay constants of Steiger and Jäger (7). Five analyses of zircon standard M257 (21) made during the session give a concordia age of 561±3 Ma when corrected using 91500 as a reference, while five analyses of OGC zircon (22) are concordant to 5% discordant and result in an upper concordia intercept of 3466±5 Ma. The analyses of three 5×5 mm areas from the DT-1 Martian zircon returned overlapping, concordant U-Pb ages corresponding to a weighted mean $^{207}Pb/^{206}Pb$ age of 1548±9 Ma. All errors of individual analyses are presented at 1s level (Table S3), while average ages are given with 95% confidence level of uncertainty (Fig. S12). The approximate position of the U-Pb rasters for the DT-1 zircon are shown in Fig. S13.

In situ Lu-Hf systematics of zircon of the DT-1 zircon. Hf isotope data were acquired at the Geochronology and Tracers Facility, British Geological Survey, using a ThermoScientific Neptune Plus MC-ICP-MS coupled to an ESL NWR193UC 193nm excimer laser ablation system equipped with a TV2 low-volume ablation cell. Ablation used a fluence of 8.3J.cm-2, 10Hz repetition rate, 15um spot size and a 15 second ablation duration whilst rastering the ablation spot along a 30-35um long line at 2um/sec scan speed for one pass. A helium gas flow through the cell of 0.6l/min was combined with the output of a Teledyne-CETAC Aridus II desolvating nebuliser approximately half-way along the sample line to provide ca.0.7l/min make-up gas to the sample line. The instrument was tuned for low UO/U and analysis performed using a static acquisition routine acquired in a time-resolved manner using 0.262 second integrations. Data were processed using the Iolite (v.3.65) data reduction software (10) and normalised using 91500 as the primary reference material and adopting the Lu/Hf and Hf isotope compositions of Wiedenbeck *et al.* (11). Corrections were performed using the Hf mass bias and a modified Yb ratio pre-calibrated for the difference in mass bias between Hf and Yb using solutions, and validated using laser ablation to demonstrate a 1:1 relationship within uncertainty between this method of correction and that using an Yb mass bias determined through the measurement of Yb isotopes. The former method is considered more beneficial and accurate as the measurement precision of the Hf mass bias is higher due to higher Hf concentrations and for the same reason is less prone to MREE oxide interferences than Yb. Validation data for GJ1 and Mud Tank zircons were $^{176}Hf/^{177}Hf$=0.282008 ±0.000020 (MSWD=1.3, n=10; εHf = -14.00±0.79) and $^{176}Hf/^{177}Hf$ = 0.282503±0.000013 (MSWD=0.85, n=10; εHf = 6.36±0.58), respectively. Although sample REE/Hf was around 5 times higher than GJ1, sample Yb/Hf was still relatively low at <0.05. The correction mechanisms described have been previously determined in the BGS-GTF lab to be effective to Yb/Hf >0.2. All uncertainties are 2s but without propagation for a long-term reproducibility. εHf calculations and uncertainties use the calculations of Ickert (23) and include propagations for uncertainties for the ^{176}Lu decay constant and CHUR values (13,14). Lu-Hf data for DT-1 and standards are reported in full in Table S4. The approximate position of the laser ablation track relative to the U-Pb rasters for DT-1 is shown in Fig. S13.

X-ray microfluorescence and Laue microdiffraction experiment of the DT-1 zircon. To demonstrate the crystallinity of the DT-1 zircon, we conducted a combined X-ray microfluorescence and Laue microdiffraction experiment of the grain before polishing and acquisition of the U-Pb and Lu-Hf data. For the X-ray measurements, the zircon grain was fixed on a quartz glass capillary (diameter 100 µm, wall thickness 10 µm, Hilgenberg GmbH, Malsfeld, Germany) with cyanoacrylate superglue (Loctite precision) under a long working distance stereomicroscope. The procedure was the same as that used in (24,25), with the addition of a micromanipulator system to facilitate handling of the sample. The X-ray experiment was carried out on beamline 34-ID-E (26) of the

Advanced Photon Source (APS) at Argonne National Laboratory. The sample was first scanned in Laue microdiffraction mode, using a polychromatic X-ray beam of up to 30 keV energy, with 2 mm Al filtering to reduce dose to the sample from low-energy X-rays. The entire zircon grain was covered with a 28-by-19-point raster (W x H), using a step size of 2 μm in the horizontal and 5 μm in the vertical direction and 2 s exposure time per point. Laue diffraction patterns were collected on a Perkin-Elmer 1621 amorphous silicon detector situated above the sample at 90 degrees to the incident beam. Next, the beamline was switched to monochromatic mode with X-ray energy of 17.4 keV, and the zircon was scanned in a 55-by-91 point raster with 1 μm x 1 μm step size and 2 s exposure time per point. Fluorescence X-rays emitted by the sample were recorded using a Hitachi Vortex silicon drift detector, with counts saved in regions-of-interest (ROIs) around the K-alpha fluorescence lines of Ca, Fe, Ni, Cu, Ti, Rb, Sr, Y and Zr and L-alpha fluorescence lines of Hf, Dy, and U. Igor Pro 8 software (Wavemetrics Inc., Lake Oswego, OR, USA) and the LaueGo software package were used for data reduction.

Supplementary Text

Petrology and mineral chemistry of basaltic clast C27. Clast C27 is a basaltic polymineralic rock fragment identified in three adjacent ~1.3-mm thick cut sections of NWA 7533. The clast was extracted from two of the thick sections using a dry-operated 250-micron diamond-coated wire saw at the Centre for Star and Planet Formation, University of Copenhagen. The largest of the two fragments was subjected to a complete breccia matrix removal and used for destructive sampling, including zircon separation. The other fragment was mounted in epoxy and used for an *in situ* chemical and mineralogical study of the clast. Clast C27 is a fine-grained, holocrystalline fragment characterized by igneous textures and a basaltic major element composition (Table S2). The clast mainly consists of plagioclase and pyroxene minerals, which are present in subequal amounts. Accessory phases constitute about 5 vol.% of the clast and include Cl-apatite, Fe-rich oxides and zircon. Plagioclase grains typically appear as oikocrysts that are poikilitically enclosing chains of sub- to euhedral grains of pyroxene, apatite and Fe-rich oxide (Figs. S14 and S15). These chains are commonly associated with grain boundaries that meet at 120° angles. Plagioclase analyses exhibit a range in anorthite component (An%) from 35.1% to 51.7% (Fig. S16, Table S6). The pyroxene grains typically measure between 20 and 80 μm in the longest dimension and are mostly subhedral to anhedral. Pyroxene minerals observed in clast C27 are pigeonite, augite and a few orthopyroxenes (Fig. S16, Table S6). Apatites in clast C27 are Cl-rich (Fig. S16, Table S8). Apatite grains are typically euhedral to subhedral and exhibit a size range from 30 to 70 μm. A euhedral, hexagonal apatite with pyroxene and Fe-rich oxide inclusions is seen in Fig. S15, panel C. Clast C27 contains trace amounts of Fe-rich oxides. Both BSE imaging and quantitative analyses of larger Fe-oxide grains (up to 30 μm in the longest dimension) indicate that these are typically Cr-bearing magnetite with bands of exsolved ilmenite (Fig. S15). Silicate grain boundaries and fractures or deformation planes in pyroxene are typically associated with submicron beads of Fe-rich oxide. Altogether, the mineralogy, textural features and major element geochemistry of clast C27 indicate that this is a fragment of an igneous basaltic rock. Geochemically and petrographically, clast C27 is similar to *Clast 5* ("basalt clast") described by Santos *et al*. (27) and *7533-1-obj2* ("microbasalt") described by Hewins *et al*. (28).

U-Pb systematics of the young zircon population. U-rich, metamict zircons or zircons with metamict domains have been previously identified in NWA 7034/7533 (29,30,31). These grains are characterized by exceedingly high U concentration of more than 10,000 ppm in some cases, resulting in appreciable radiation damage and amorphous textures. The U-Pb systematics of these grains are well-understood. Namely, the metamict zircons typically plot along a discordia line with upper and lower intercepts of ~4.4 Ga and ~1.5 Ga, respectively. As such, these grains are interpreted to reflect an ancient zircon population that have experienced partial or complete resetting of their U-Pb systematics during a transient thermal event experienced by the protolith material to the meteorite breccia. This interpretation is supported by the U-Pb systematics of individual phosphate minerals (32) as well as the whole-rock Ar-Ar systematics of NWA 7034 (33), which point to thermal events between ~1.5 and ~1.3 Ga. We note that no metamict zircons with ages younger than ~1.5 Ga have been identified in these meteorites using in situ methods. This is also consistent with the whole rock Ar-Ar systematics of the 7034 meteorite breccia, indicating that

the host meteorite has not experienced significant thermal events between 1.3 Ga and the final assembly/brecciation after 225 Ma (33).

In contrast to the amorphous, metamict grains identified in earlier studies, the young zircon population we report are clear and mainly colourless grains (Fig. S4), attributes that are associated with more crystalline zircons in which diffusional rates are exceedingly slow even at elevated temperatures. This is inconsistent with near complete loss of Pb from ancient zircons that would be required to reset ancient zircons to produce the range of young ages (~1.2 Gyr) that are now concordant to near-concordant. Indeed, six of the young zircons record concordant U-Pb systematics within uncertainties (Fig. 1d). Resetting of all eight zircons over ~1.2 Gyr requires that there were multiple thermal events spanning this period that were significant enough to fully reset these zircons individually prior to their incorporation into this meteorite. This is considered to be extremely unlikely given the lack of any other evidence for thermal pulses, including the thermally sensitive Ar-Ar system (*8*), affecting components of this meteorite after 1.3 Ga. Critically, the Laue diffraction patterns obtained for the DT-1 zircon confirms that this grain is not metamict, in line with its low U concentration of ~10 ppm (Table S3). This firmly establishes the existence of young zircons in NWA 7034/7533 that record primary crystallization ages that are unrelated to the previously described metamict zircon population with disturbed U-Pb systematics. Finally, the chondritic initial Hf isotope compositions of the young zircon population identified here provide additional support that their U-Pb ages reflect primary crystallization of the grains. Indeed, it is not possible to consistently produce young concordant to near-concordant U-Pb ages for zircons with chondritic Hf isotope compositions around zero (i.e. εHf ~0) by resetting ancient zircons that were thermally reset at random times in their evolution. If the U-Pb ages of these grains were essentially reflecting a late stage disturbance of the systematics, the Hf isotope signal of the zircons is predicted to be dominated by that acquired at the time of the original crystallization of the grains at ~4.4 Ga given that Hf is a major and immobile element in zircon. We calculate that ancient zircons would have εHf values of –70 to –100 by 300 Ma (Fig. S10) and there is no mechanism that would reset the εHf values of each zircon to ~0 at the time of their respective resetting events. This estimate is robust and insensitive to significant modification of the Lu/Hf ratio, which has been varied from 0 to 0.0065 (the highest ratio observed in a young zircon) in these calculations. As such, we conclude that the U-Pb ages of the young zircon are primary crystallization ages and that their Hf isotope compositions reflects that of their source reservoirs.

Model of zircon saturation. To investigate whether or not zircon is predicted to crystallize from an evolving mafic magma, we modelled the fractionation of a Martian basalt derived from the deep mantle. As a starting composition, we use the experimental melt composition DW23 formed by melting the estimated bulk silicate composition of Mars (34) at 2 GPa and 1500ºC (35). We fractionate this composition at low pressure (0.1 GPa) over ten steps, in each case crystallising 10% of the starting volume and removing the solid (mineral) fraction, before recalculating a new melt composition as a starting point for the next step. All calculations were performed via thermocalc 3.50 (36) using the thermodynamic models of Holland *et al.* (37) [see also (38)], which enable calculation of subsolidus to suprasolidus (melt-bearing) phase equilibria for bulk compositions ranging in composition from peridotite to granite. Although these models permit calculations in the K_2O–Na_2O–CaO–FeO–MgO–Al_2O_3–SiO_2–H_2O–TiO_2–Fe_2O_3–Cr_2O_3 (KNCFMASHTOCr) chemical system, we use an anhydrous and ferric iron-free subset (i.e., in the KNCFMASTCr system) that is appropriate to Martian compositions. All software required for the calculations is available at: https://hpxeosandthermocalc.org/.

Melt evolution during fractional crystallisation

The starting composition (DW23; Stage 0) and calculated compositions of the fractionated melts (stages 1–10) in terms of weight percent oxides are given in Table S9. The compositions of melt and the minerals predicted to form in equilibrium with melt at each step, in terms of mol.% oxides are provided in Table S10, along with the composition (X) of the phases in which X_{Ol}, X_{Pig}, X_{Cpx} and X_{Liq} are atomic Mg/(Mg + Fe), X_{Spl} is atomic Cr/(Cr + Al), and X_{Pl} is atomic Ca/(Ca + Na + K). For the modelled starting composition at 0.1 GPa, olivine is predicted to appear on the liquidus at 1519 ºC and reaches a mode of 10% at 1458ºC (Table S10). Thereafter, the sequence of appearance

of minerals is spinel (chromite) during step 3 at 1272 ºC, plagioclase during stage 4 (1117 ºC), pigeonite at stage 5 (1086 ºC), clinopyroxene at stage 6 (1063 ºC), ilmenite at stage 7 (1039 ºC) and quartz at stage 9 (924 ºC) prior to crossing the solidus at 889 ºC. Spinel is not predicted after stage 5, olivine after stage 6, pigeonite after stage 7 and ilmenite after stage 9. The predicted occurrence of quartz during stages 9 and 10 indicates $a SiO_2 = 1$, a requirement for zircon (rather than baddeleyite) growth.

Zircon saturation and Zr concentrations in the model melts

Fractionation model results have been used to estimate zircon saturation concentrations at each of ten fractionation steps, using melt compositions and temperatures shown for each step in Tables S9 and S10 and the experimentally defined equation described by Shao *et al.* (39). Zr concentrations at each step have been determined assuming chondritic Zr concentration (of about 10ppm) in the original Martian mantle, which results in about 40 ppm in the basaltic melt formed by 25% equilibrium melting of this mantle. The following increase of Zr content in the melt has been modelled using mineral fractions in coexisting solid shown for each step in Table S9 and Zr partition coefficients from GERM database (https://earthref.org/KDD/e:40/). Both zircon saturation concentrations and Zr concentrations in evolving melt are shown in Fig. S11, which suggests that zircon can start to crystallise when around 3% of the original melt is left. This melt will likely exist as small interstitial pockets in mafic rocks. Thus, model calculations suggest that originally low Zr basaltic melts can form zircon at the very last stages of fractional crystallisation.

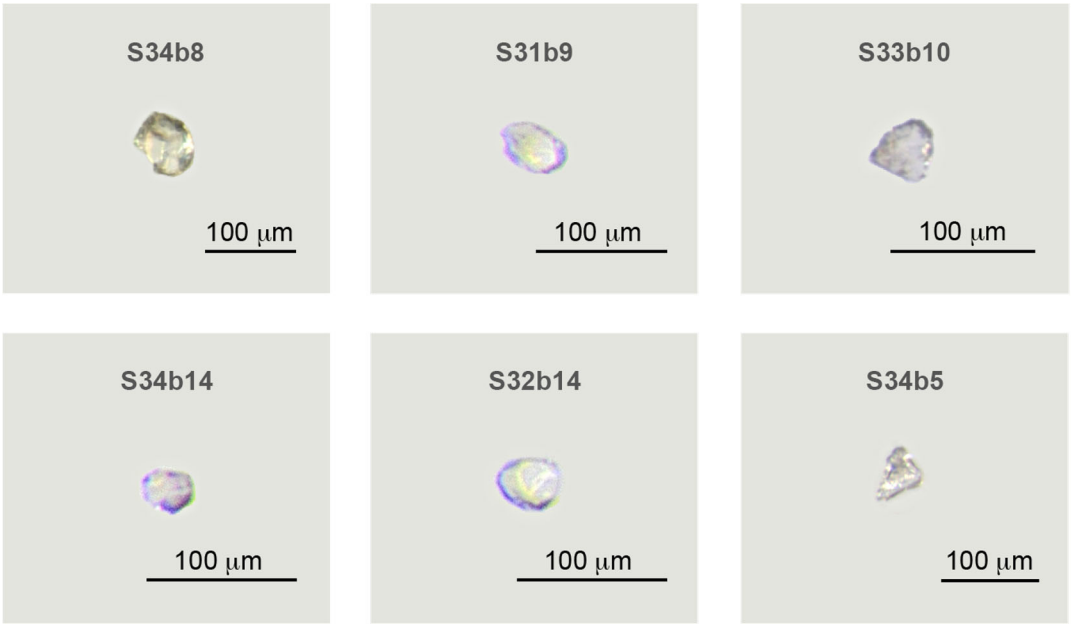

Fig. S1. Photomicrographs of a representative sample of the NWA 7533 ancient (>4300 Ma) zircon population analyzed in this study taken under natural light.

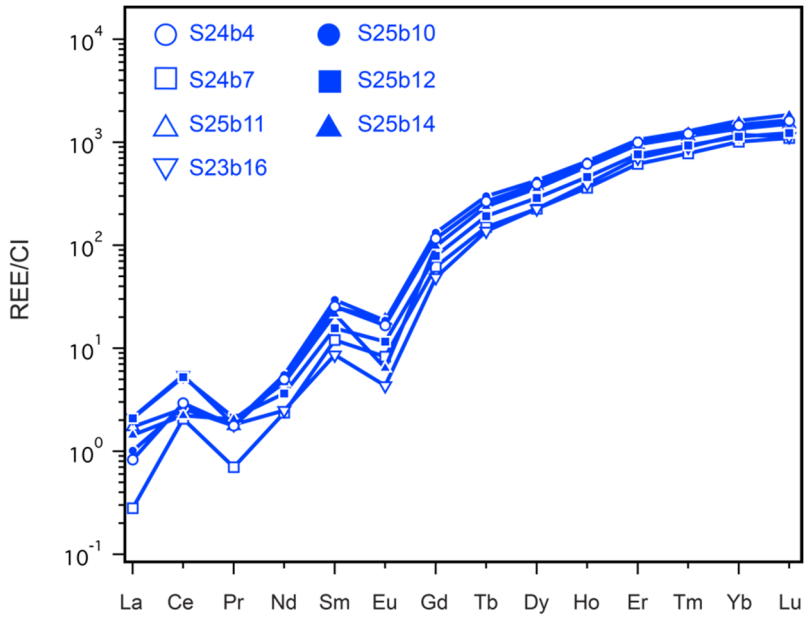

Fig. S2. Chondrite normalized Rare Earth Elements (REEs) abundances of a subset of the zircons analyzed in this study, obtained on the same zircon volume as that used for the U-Pb systematics. Data used in this figure are reported in Table S8. Note that the U-Pb ages for grains S24B4, S24B7 and S25B10 are reported in Bouvier *et al.* (1).

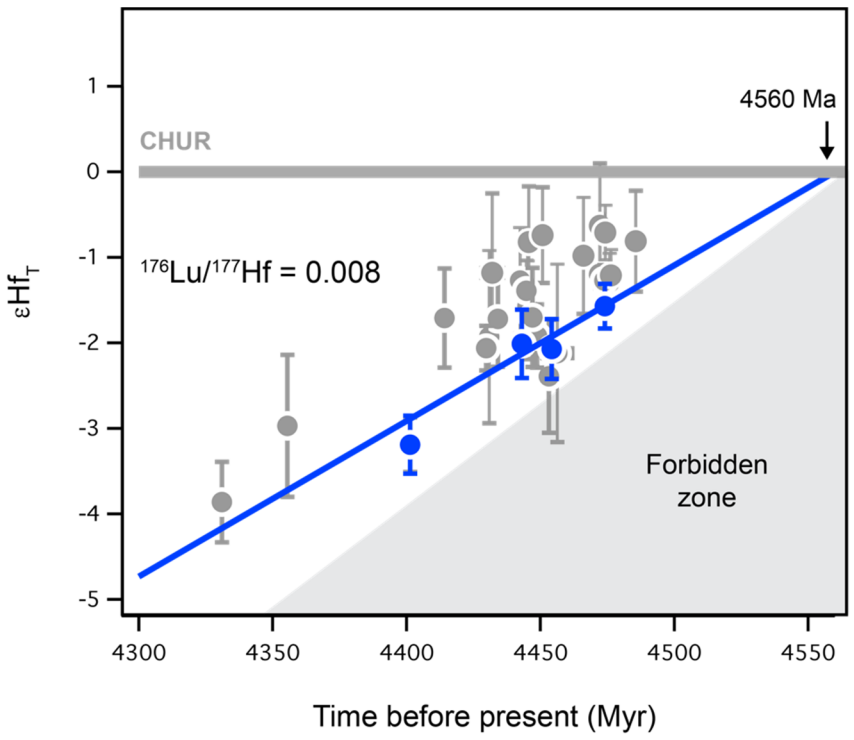

Fig. S3. Hf isotope evolution diagram depicting the most unradiogenic zircons from the NWA 7034 and 7533 meteorites.

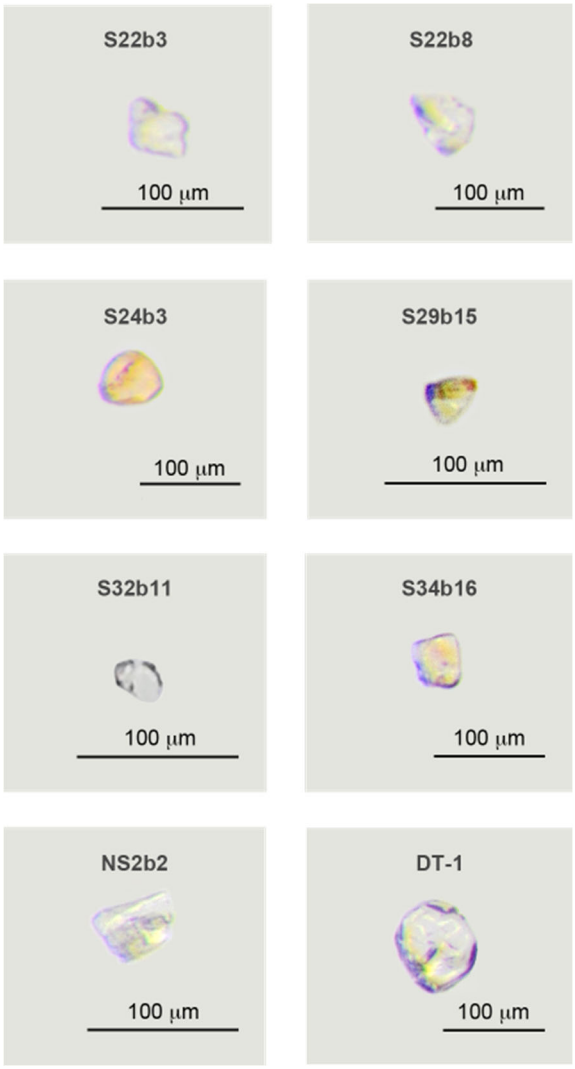

Fig. S4. Photomicrographs of the NWA 7533 young (<1600 Ma) zircon population identified in this study taken under natural light.

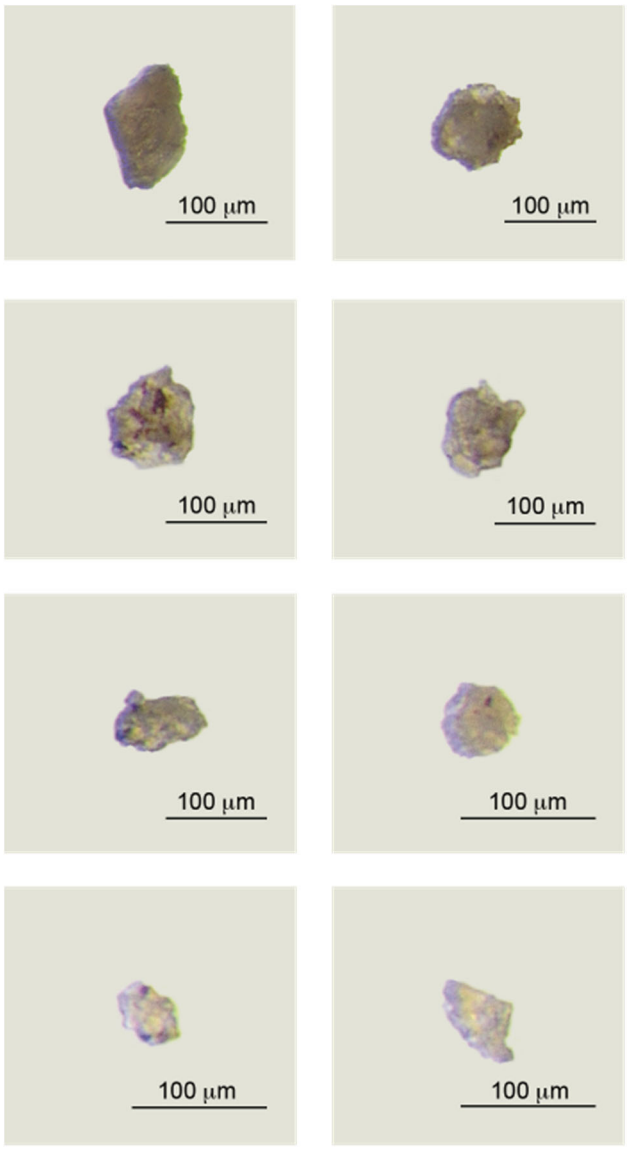

Fig. S5. Photomicrographs of selected metamict zircons from NWA 7533 identified in this study taken under natural light and not selected for analysis.

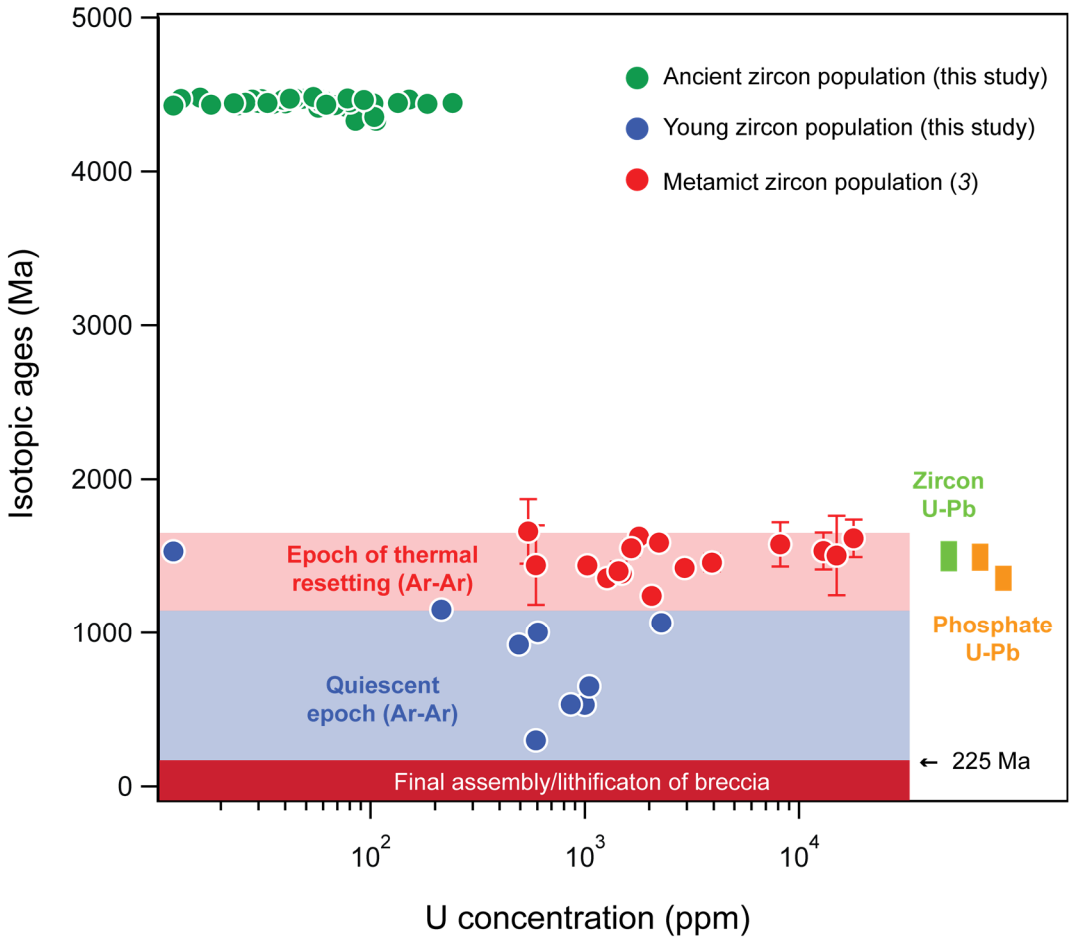

Fig. S6. Age and U concentration of various zircon population identified in NWA 7034/7533. The thermal history of the meteorite breccia. namely the epoch of thermal resetting and quiescent period. are based on Ar-Ar chronology (33). The zircon U-Pb age on the right-hand side of the diagram is the concordia age for the metamict zircon population (29). Concordia ages of phosphates from NWA 7034/7533 (29, 32) are also indicated. Final assembly/lithification of the breccia is inferred based on noble gas systematics to have occurred after 225 Ma (33).

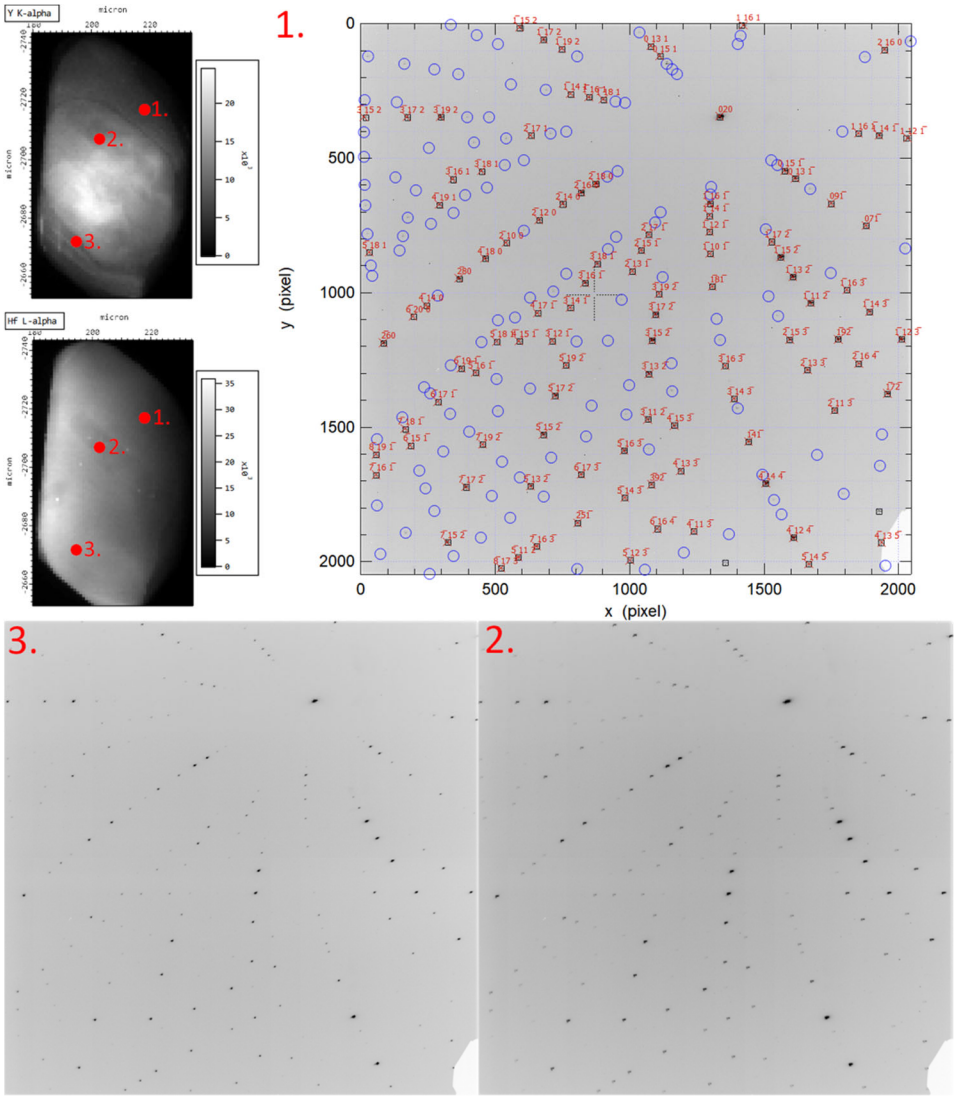

Fig. S7. Laue microdiffraction experiments. The top left panels are X-ray fluorescence maps of the DT-1 zircon. indicating the Y (above) and Hf (below) distribution. The grayscale in these images corresponds to total counts of the indicated fluorescence line. Also indicated in red are the positions where the three shown Laue diffraction patterns were acquired. Clockwise from top right: the Laue diffraction patterns corresponding to spots 1-3 in the fluorescence maps. White corresponds to zero counts and black to 2178 counts. The overlay on pattern 1 shows the indexing of the zircon crystal. Peaks marked by squares are those used for indexing, with their associated Miller indices. Blue circles indicate expected positions of the remaining (often very weak) peaks. All three Laue patterns are essentially identical, with sharp peaks indicating that the zircon is crystalline and the same indexing applies to all three positions.

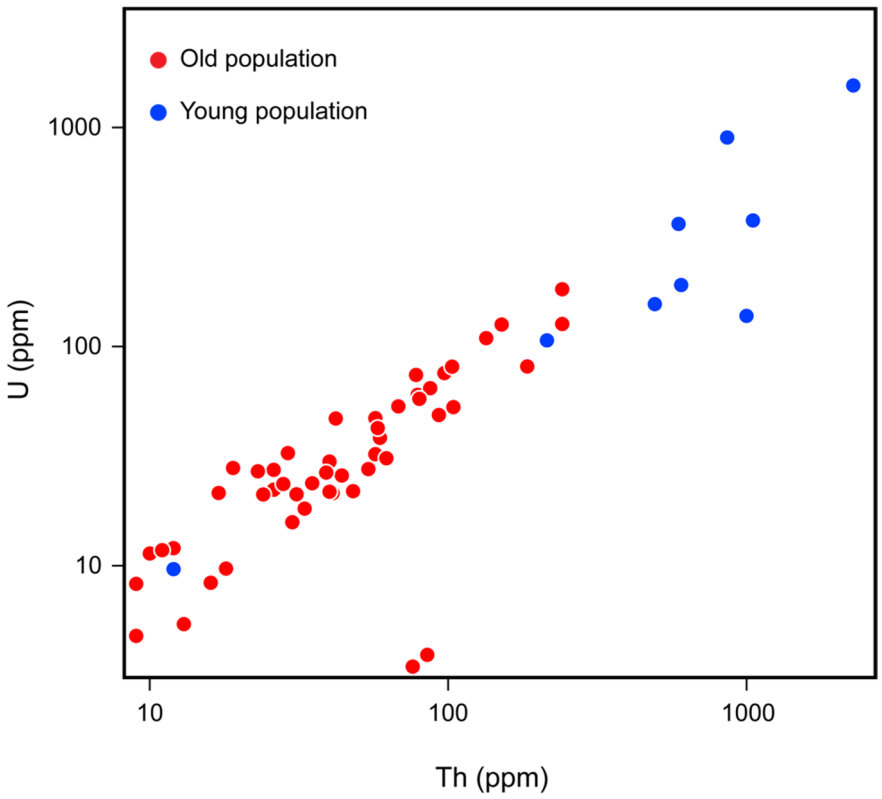

Fig. S8. Th and U concentrations of young (<1.5 Ga) and old (>4.3 Ga) zircon populations from the NWA 7533 investigated in this study.

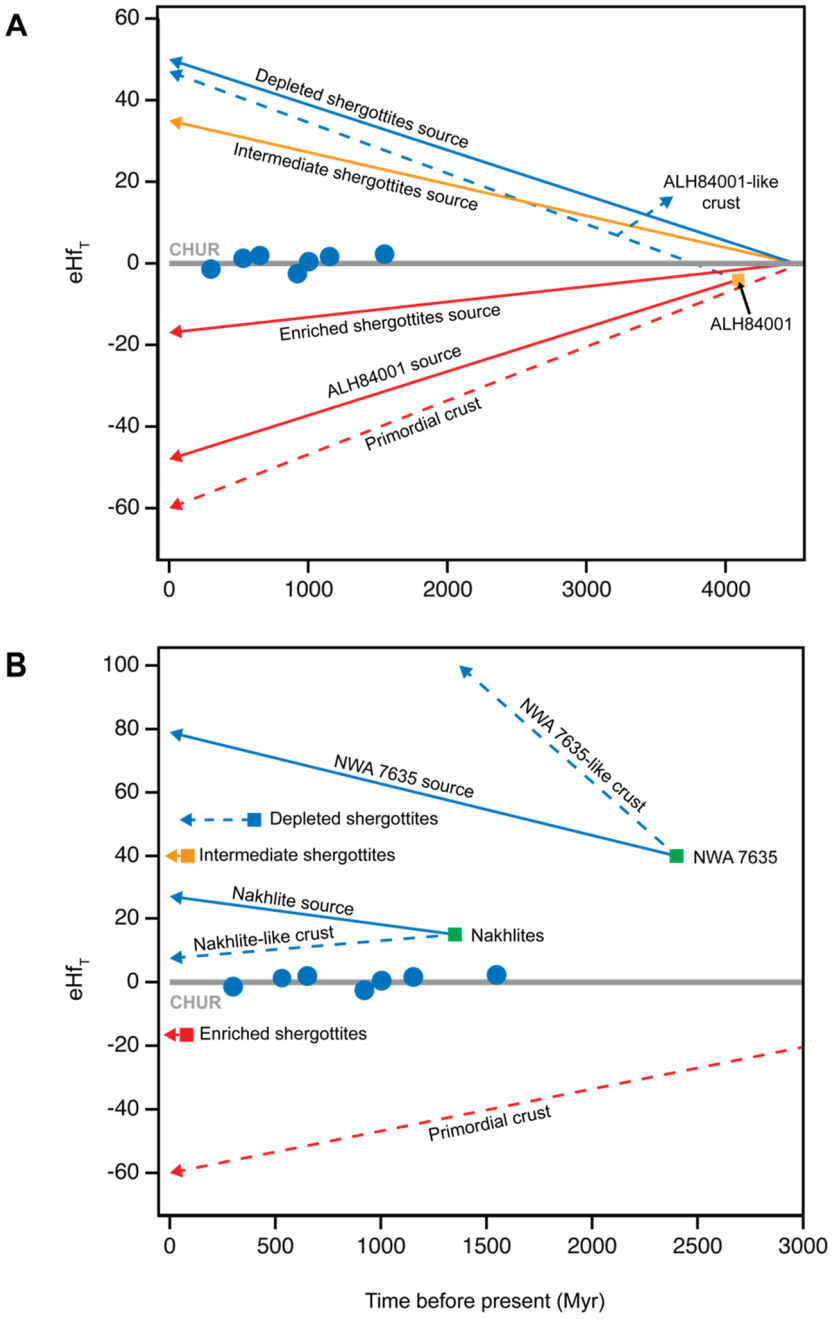

Fig. S9. Hf isotope evolution diagrams of known Martian mantle (solid) and crustal (stippled) reservoir plotted together with the young zircon population identified here. In (**A**), we show the time evolution of ancient (>3 Ga) mantle and crustal reservoirs. In (**B**), we depict the time evolution of mantle and crustal reservoirs formed within the last 3 Ga. Given the relatively young ages of shergottites, remelting of shergottite-like crusts does not result in drastically different Hf isotope compositions. Note that none of the existing Martian crustal and/or mantle reservoirs evolve to a composition that is consistent with that of the young population identified here. Source data from refs. (40-46).

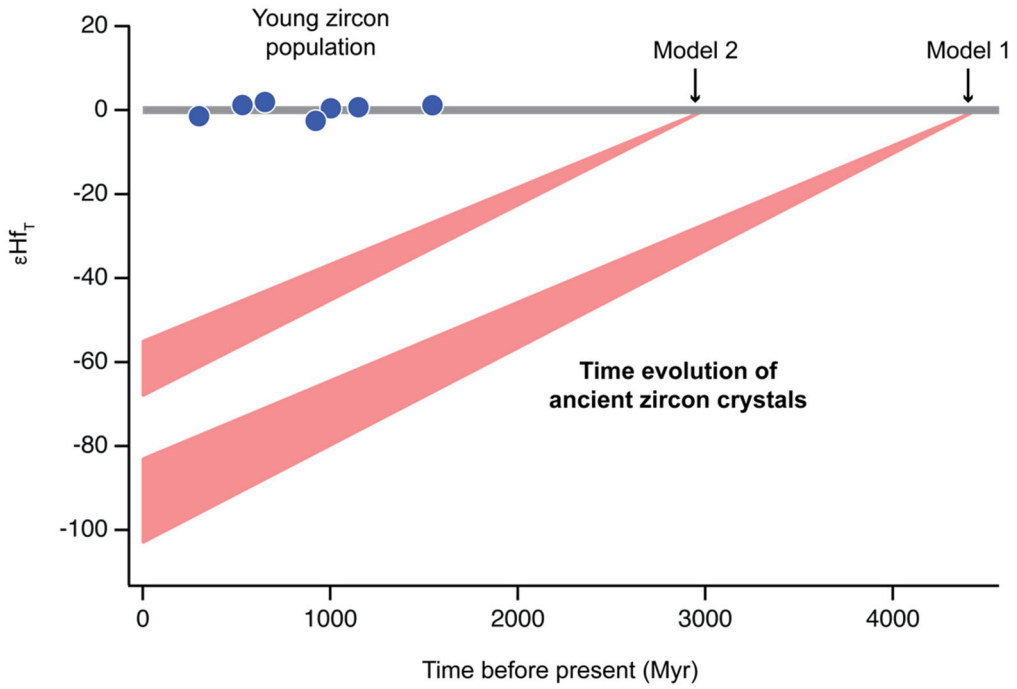

Fig. S10. Hf isotope evolution diagram. We show the time evolution of ancient zircon crystals formed at two epochs from a primitive reservoir. namely at ~4450 Ma (model 1) and ~3000 Ma (model 2). The $^{176}Lu/^{177}Hf$ values were varied from 0 to 0.0065. the later representing the highest value measured for a zircon in this study. Model 1 is more realistic as it is based on observed ages of ancient zircons. No age data of ancient zircons exist that would support model 2. In either case, the Hf isotope composition of the young zircon population is not consistent with the hypothesis that their U-Pb ages reflect thermal resetting of ancient zircons. The grey line represents the CHUR composition.

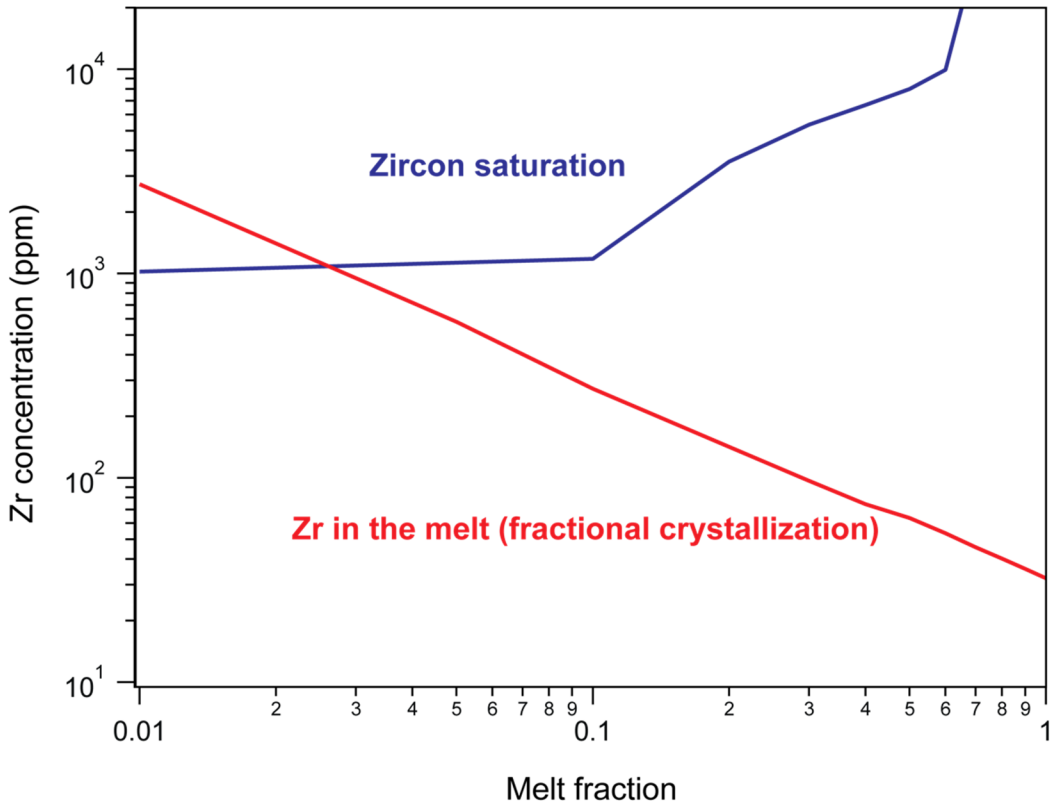

Fig. S11. Zircon saturation concentration and Zr content of an evolving basaltic melt. Zircon saturation occurs after 97% fractional crystallization. See Supplementary Text for details.

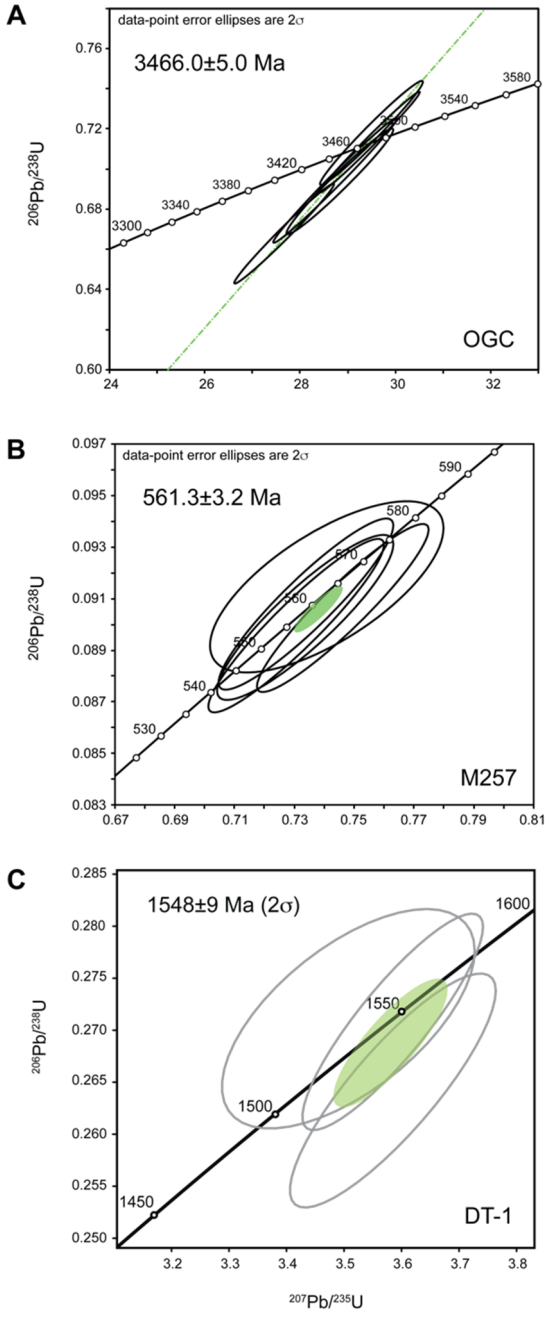

Fig. S12. U-Pb concordia diagrams for the spot analyses of the OGC (**A**) and M257 (**B**) zircon standards as well as the DT-1 zircon (**C**) obtained by SIMS. Labels on the concordia curve represent time before present. Data point error ellipses are 2σ. The green line in A represents the upper concordia intercept while the green ellipse in (**B)** and **(C)** reflects the weighted mean age. Data reported in full in Table S3.

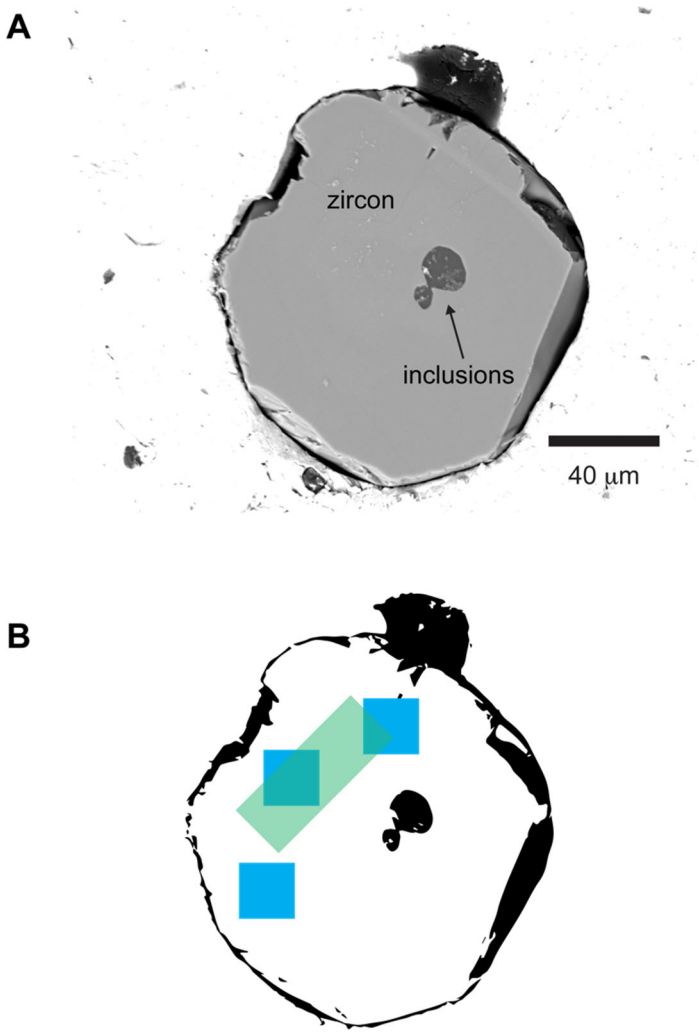

Fig. S13. Various representations of the DT-1 zircon, including its inclusions. Shown in (**A)** we show a back scattered image of the DT-1 zircon after initial polishing. In (**B)**, we show the approximate location of the U-Pb rasters (blue) and Lu-Hf laser ablation track (green).

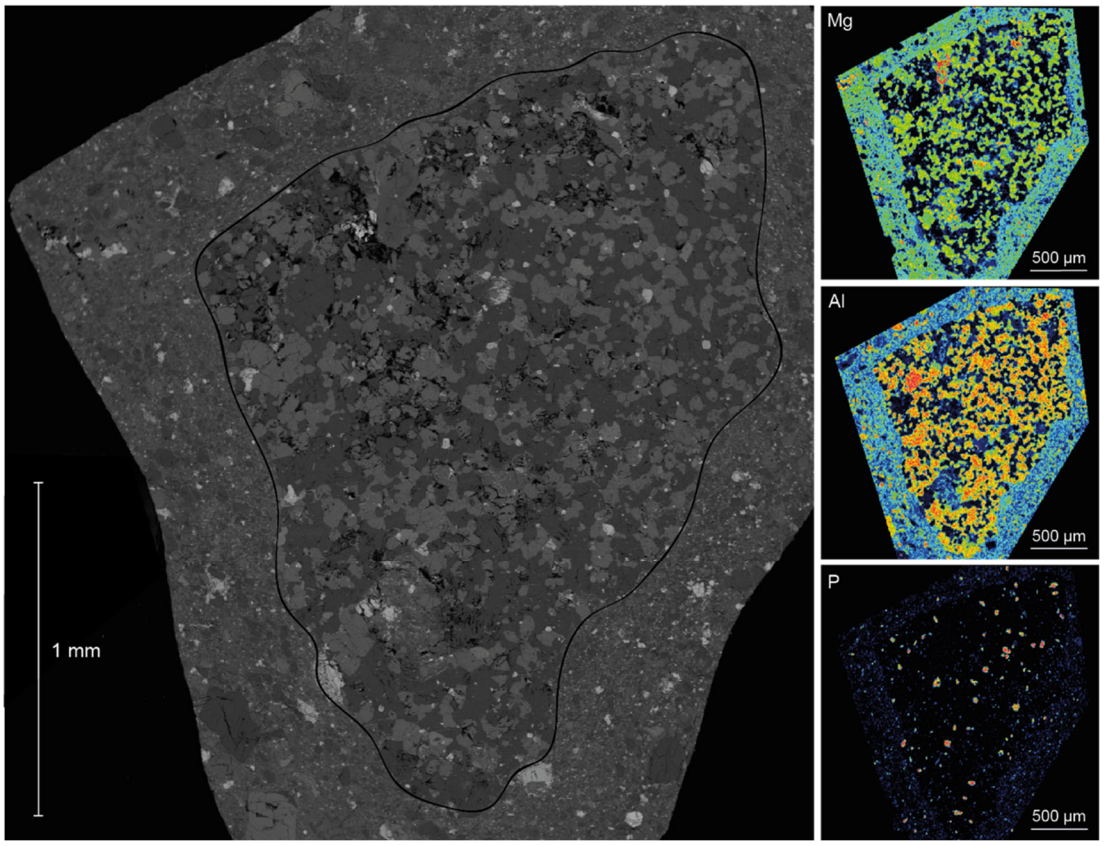

Fig. S14. Left panel) Backscattered electron image of clast C27. Black solid line marks the clast-breccia boundary. Right panels) Magnesium, Al and P element maps of clast C27. Warmer colors indicate a higher relative concentration.

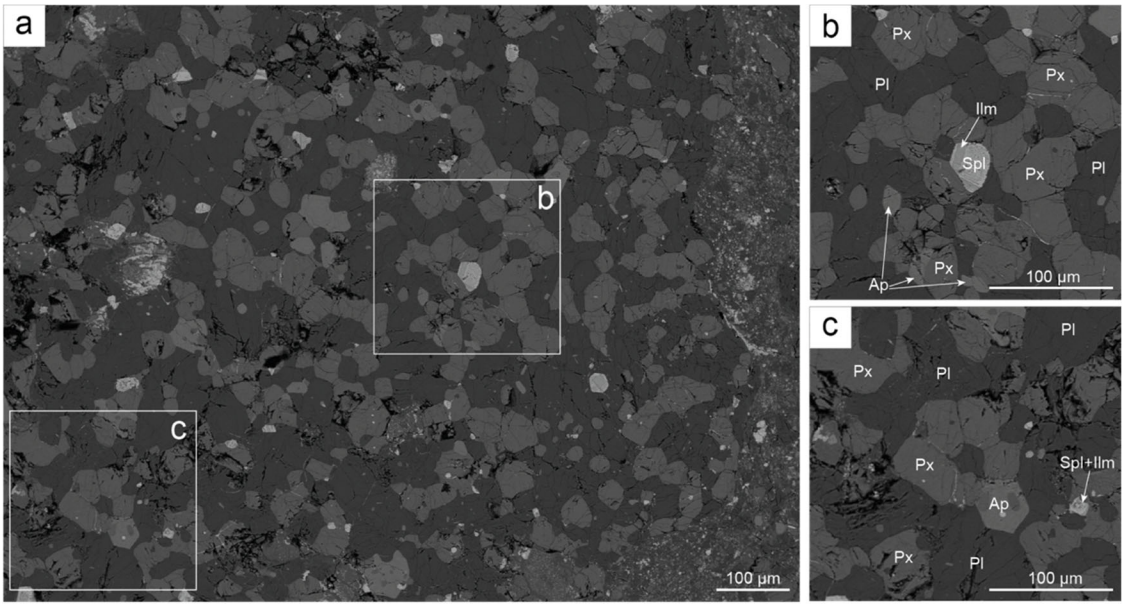

Fig. S15. Backscattered electron images showing textural features in clast C27. (**A**) Clast C27 exhibits a subophitic texture. (**B**) Chains and clusters of pyroxene, apatite and Fe-rich oxides. Bands of exsolved ilmenite appear in the spinel in the center of the image. (**C**) A chain of pyroxene and euhedral apatite (containing inclusions) is poikilitically enclosed by plagioclase. Px, pyroxene. Pl, plagioclase, Ap, apatite, Ilm, ilmenite and Spl, spinel.

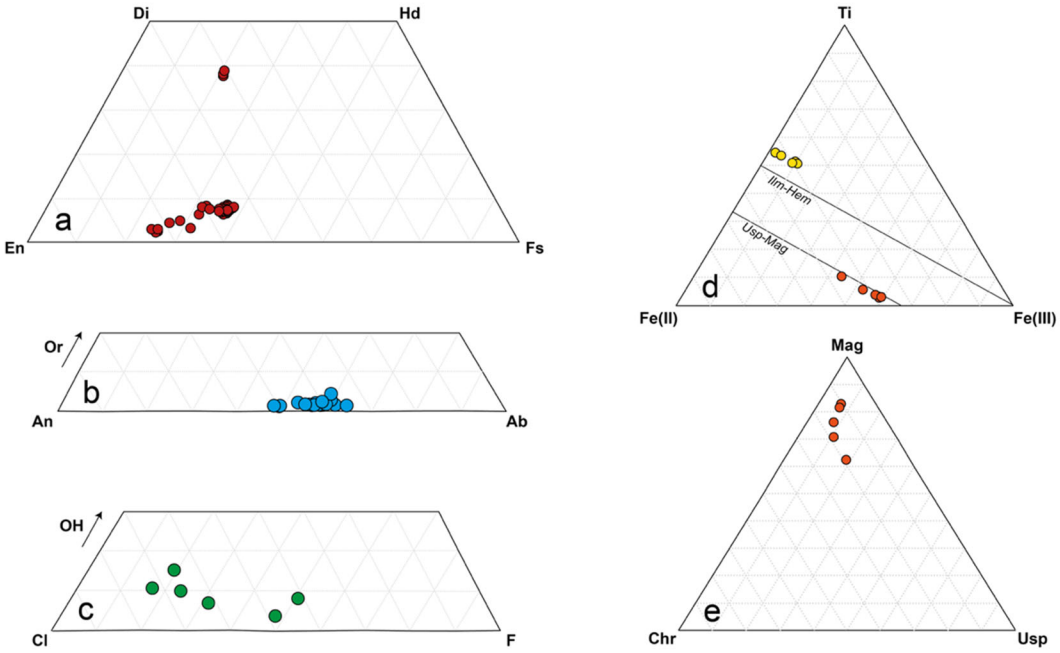

Fig. S16. Clast C27 mineral composition diagrams. (**A**) Clast C27 pyroxene compositions plotted in the quadrilateral pyroxene end-member diagram. Orthopyroxene, pigeonite and augite are present in clast C27. (**B**) Clast C27 feldspar compositions plotted in the ternary feldspar end-member diagram. Feldspars range in An% from 35.1% to 51.7% (orthoclase content <5%). (**C**) Clast C27 apatite compositions plotted in a ternary OH-Cl-F discrimination diagram. Apatite in clast C27 is Cl-rich. (**D**) Clast C27 Fe-rich oxides plotted in a ternary Ti-Fe(II)-Fe(III) discrimination diagram. Spinel (orange points) with ilmenite (yellow points) exsolution bands appear in the clast. (**E)** The same spinel analyses as in (**D**) plotted in the ternary Mag-Chr-Usp end-member diagram. Spinels in clast C27 are Cr-bearing magnetite.

Table S1. $^{207}Pb/^{206}Pb$ age data and ^{176}Lu-^{176}Hf systematics of the NWA 7533 old zircon population.

Sample	$^{207}Pb/^{206}Pb$ age (Ma)	$^{176}Lu/^{177}Hf$	$^{176}Hf/^{177}Hf$	$^{178}Hf/^{177}Hf$	$^{180}Hf/^{177}Hf$	εHf_T
S28b16	4472.2±3.0	0.000476	0.279883±20	1.46722±4	1.88671±9	−0.61±0.73
S29b13	4331.0±1.4	0.000044	0.279851±13	1.46720±3	1.88668±7	−3.87±0.47
S31b9	4414.1±1.0	0.000699	0.279911±16	1.46717±5	1.88661±10	−1.70±0.58
S32b10	4453.2±1.3	0.000887	0.279882±18	1.46717±3	1.88665±9	−2.40±0.66
S32b12	4466.0±1.1	0.001760	0.279989±18	1.46719±4	1.88651±10	−0.98±0.68
S32b13	4355.4±1.4	0.001046	0.279944±23	1.46719±2	1.88668±8	−2.99±0.84
S32b14	4445.6±2.0	0.000575	0.279904±18	1.46719±6	1.88679±10	−0.83±0.66
S33b4	4450.8±2.2	0.000855	0.279927±15	1.46718±3	1.88659±9	−0.74±0.55
S24b6	4401.3±0.5	0.000875	0.279893±9	1.46717±2	1.88662±5	−3.19±0.32
S23b10	4454.2±0.7	0.000364	0.279845±10	1.46717±2	1.88694±6	−2.08±0.36
S28b3	4442.4±1.4	0.000880	0.279920±17	1.46719±3	1.88662±10	−1.26±0.62
S28b4	4445.2±1.3	0.000699	0.279894±17	1.46715±4	1.88676±9	−1.59±0.62
S28b7	4445.2±0.5	0.001403	0.279955±14	1.46720±3	1.88667±8	−1.55±0.53
S28b8	4472.2±2.1	0.000685	0.279885±12	1.46719±3	1.88662±6	−1.22±0.46
S28b2	4456.0±5.6	0.000637	0.279866±28	1.46719±6	1.88675±10	−2.11±1.03
S33b10	4430.9±2.9	0.001314	0.279967±25	1.46722±6	1.88681±12	−1.16±0.92
S30b3	4430.9±2.9	0.000485	0.279875±28	1.46725±7	1.88804±14	−1.94±1.01
S34b5	4485.5±2.2	0.000729	0.279891±16	1.46725±6	1.88685±27	−0.82±0.59
S34b7	4475.8±1.1	0.000331	0.279849±9	1.46719±2	1.88668±5	−1.27±0.33
S34b8	4444.7±1.3	0.000265	0.279862±10	1.46716±5	1.88663±30	−1.39±0.37
S34b13	4434.1±1.1	0.000730	0.279900±15	1.46720±5	1.88689±28	−1.72±0.56
NS2B3	4443.7±1.2	0.000350	0.279853±11	1.467148±2	1.88663±49	−1.99±0.40

Age uncertainties are 2σ. Hf isotope ratios are reported normalized to the composition of the JMC-475 Hf standard. Uncertainties on the Hf isotope ratios reflect the 2-standard-error internal precision in the last decimal places. U–Pb data are reported in full in Dataset S1.

Table S2. Major and selected trace element composition of basalt clast C27 as well as that of reference material BHVO-2.

Method	BHVO-2G SEM (wt.%)	BHVO-2 SEM + ICPMS (wt.%)	C27 SEM + ICPMS (wt.%)	Method	BHVO-2 SEM + ICPMS (ppm)	RDS (%)	C27 SEM + ICPMS (ppm)	RDS (%)
Na_2O		2.24	2.97	La	14.6	0.6	6.2	2.8
MgO	7.27	7.27	8.01	Ce	36	1.0	15	0.3
Al_2O_3		13.5	11.4	Pr	5.0	1.0	2.1	2.5
SiO_2	49.1	49.1	50.8	Nd	24	1.8	10	1.7
P_2O_5		0.29	1.74	Sm	6.0	3.1	2.7	8.6
K_2O		0.52	0.21	Eu	1.9	2.6	0.9	1.9
CaO		11.3	6.7	Gd	6.1	3.9	3.2	12.5
TiO_2		2.70	0.55	Tb	0.94	2.7	0.53	8.2
Cr_2O_3		0.041	0.147	Dy	5.2	1.3	3.3	9.3
MnO		0.169	0.286	Ho	0.93	1.5	0.68	4.5
FeO		11.02	11.43	Er	2.4	0.6	2.0	7.7
Mg#		54.0	55.54	Tm	0.33	1.0	0.24	3.1
Mg/ppm		43823.5	48306.4	Yb	1.9	7.1	1.8	6.9
Fe/afu		0.34	0.36	Lu	0.28	1.4	0.22	4.3
Mn/afu		0.0053	0.0092	Hf	4.1	1.9	0.6	14.9
Na_2O+K_2O		2.8	3.2	Zr	161.40	0.5	23.7	2.1
Total		98.19	94.19					

Table S3. Secondary ionization mass spectrometry (SIMS) U-Pb data for the DT-1 zircon and two standards. Uncertainties are 1σ.

	Composition				Ratios (Pb_C corrected)							Ages (Pb_C corrected)						
Sample spot	[U] ppm	[Th] ppm	[Pb] ppm	Th/U	$^{207}Pb/^{235}U$	±s %	$^{206}Pb/^{238}U$	±s %	r	$^{207}Pb/^{206}Pb$	±s %	$^{207}Pb/^{235}U$	±s	$^{206}Pb/^{238}U$	±s	$^{207}Pb/^{206}Pb$	±s	$^{206}Pb/^{204}Pb$
DT-1 zircon																		
1	15	13	5	0.838	3.58461	1.79	0.2708	1.57	0.87795	0.09599	0.86	1546.13	14.29	1545.03	21.60	1547.63	15.99	11890.2
2	9	6	3	0.628	3.50744	2.56	0.2711	1.59	0.62032	0.09382	2.01	1528.89	20.44	1546.60	21.88	1504.47	37.48	1377.1
3	13	10	5	0.790	3.58488	2.04	0.2642	1.74	0.85239	0.09841	1.07	1546.19	16.32	1511.28	23.46	1594.24	19.78	13507.8
OGC std																		
1	16	17	18	1.060	29.49717	1.50	0.7179	1.47	0.98063	0.29798	0.29	3470.21	14.86	3488.33	39.81	3459.76	4.55	36363.5
2	40	51	46	1.279	29.46138	1.46	0.7134	1.45	0.99105	0.29951	0.19	3469.02	14.44	3471.33	38.97	3467.68	3.02	44109.5
3	21	20	22	0.953	28.73945	1.85	0.6944	1.83	0.99054	0.30018	0.25	3444.66	18.34	3399.25	48.65	3471.18	3.93	24129
4	11	9	12	0.774	28.83226	1.59	0.6938	1.56	0.97631	0.30139	0.34	3447.82	15.77	3397.16	41.23	3477.40	5.33	19919.1
5	26	20	26	0.792	27.66631	1.55	0.6680	1.53	0.98741	0.30040	0.24	3407.34	15.27	3298.00	39.54	3472.28	3.78	21690.9
M257 std																		
1	123	34	13	0.280	0.73395	1.63	0.0908	1.49	0.91857	0.05863	0.64	558.87	7.01	560.23	8.01	553.30	13.96	28701.8
2	129	36	13	0.282	0.73362	1.64	0.0903	1.45	0.88647	0.05894	0.76	558.68	7.06	557.16	7.75	564.88	16.41	33790.5
3	124	35	13	0.280	0.74625	1.57	0.0906	1.47	0.93276	0.05971	0.57	566.05	6.86	559.37	7.87	592.95	12.26	81159.1
4	140	37	15	0.263	0.74085	2.16	0.0915	1.48	0.68555	0.05875	1.57	562.90	9.37	564.20	8.00	557.68	33.89	50084.6
5	124	35	13	0.283	0.73062	1.64	0.0900	1.53	0.93172	0.05891	0.60	556.92	7.05	555.27	8.13	563.67	12.91	39765.7

Table S4. Hf isotope compositions of the 91500 zircon terrestrial standard obtained by solution mode MC-ICP-MS. Individual aliquots each contained approximately 1 ng of Hf.

Sample	$^{176}Hf/^{177}Hf$	2SE	$^{178}Hf/^{177}Hf$	2SE	$^{180}Hf/^{177}Hf$	2SE
91500-1	0.282324	0.000017	1.467146	0.000036	1.886630	0.000100
91500-2	0.282306	0.000017	1.467200	0.000032	1.886716	0.000095
91500-3	0.282301	0.000015	1.467167	0.000031	1.886640	0.000085
91500-4	0.282298	0.000013	1.467187	0.000026	1.886762	0.000086
91500-5	0.282320	0.000019	1.467184	0.000023	1.886700	0.000140
91500-6	0.282303	0.000017	1.467193	0.000036	1.886640	0.000160
91500-7	0.282319	0.000017	1.467166	0.000039	1.886686	0.000084
91500-8	0.282306	0.000021	1.467145	0.000047	1.886620	0.000130
91500-9	0.282310	0.000021	1.467206	0.000036	1.886747	0.000099
Average and 2SD	***0.282310***	***0.000017***	***1.467177***	***0.000042***	***1.886682***	***0.000099***

Hf isotope ratios are reported normalized to the composition of the JMC-475 Hf standard. Uncertainties on the Hf isotope ratios reflect the 2SE internal precision in last decimal places.

Table S5: ^{176}Lu-^{176}Hf data for terrestrial GJ1 and Mud tank zircon standard as well as the Martian DT-1 zircon obtained by LA-MC-ICP-MS. The $^{176}Hf/^{177}Hf$ ratios are reported normalized to the composition of the 91500 zircon standard. Uncertainties on the Hf isotope ratios are on the last decimal places and reflect the 2-standard-error measurement precision propagated for session-level over dispersion.

Sample	$^{176}Lu/^{177}Hf$	$^{178}Hf/^{177}Hf$	$^{180}Hf/^{177}Hf$	$^{176}Hf/^{177}Hf$
GJ1-1	0.00022626±09	1.46728±14	1.88696±21	0.282006±42
GJ1-2	0.00022750±19	1.46730±12	1.88665±25	0.282018±54
GJ1-3	0.00022610±19	1.46720±13	1.88684±23	0.281981±52
GJ1-4	0.00023204±07	1.46729±11	1.88686±26	0.282000±54
GJ1-5	0.00022940±10	1.46724±16	1.88673±26	0.282074±67
GJ1-6	0.00022490±17	1.46721±16	1.88654±21	0.281985±42
GJ1-7	0.00022170±16	1.46731±13	1.88678±28	0.281981±54
GJ1-8	0.00022750±11	1.46729±12	1.88694±31	0.281988±49
GJ1-9	0.00023117±08	1.46727±13	1.88656±26	0.282035±49
GJ1-10	0.00023357±09	1.46731±15	1.88673±25	0.282046±50
Mud Tank-1	0.00005562±4	1.46735±13	1.88688±23	0.282474±49
Mud Tank-2	0.00005602±3	1.46729±15	1.88670±28	0.282532±47
Mud Tank-3	0.00005547±4	1.46720±12	1.88671±22	0.282495±40
Mud Tank-4	0.00005542±4	1.46732±11	1.88694±28	0.282511±51
Mud Tank-5	0.00005593±3	1.46734±14	1.88690±32	0.282522±51
Mud Tank-6	0.00005582±3	1.46721±13	1.88690±19	0.282511±36
Mud Tank-7	0.00005585±3	1.46729±10	1.88698±23	0.282509±35
Mud Tank-8	0.00005461±3	1.46728±11	1.88686±20	0.282519±34
Mud Tank-9	0.00005479±4	1.46720±12	1.88670±22	0.282487±36
Mud Tank-10	0.00005487±3	1.46723±10	1.88678±21	0.282475±40
DT-1	0.001173±85	1.46711±12	1.88663±21	0.281898±38

Table S6. Representative electron microprobe analyses of feldspar, pyroxene, spinel and ilmenite in clast C27.

Analysis label	L4 467	L5 472	pt26	L7 1414	pt10	pt42	L11 1487	pt35	pt02	pt01	pt03	pt25
Element oxides (wt%)												
SiO_2	59.10	56.00	57.69	51.25	53.39	54.00	0.84	0.20	0.08	1.01	0.30	0.25
Al_2O_3	24.74	26.76	26.14	1.30	0.39	1.43	1.16	1.83	2.03	0.23	0.08	0.01
TiO_2	0.08	0.04	0.06	0.61	0.34	0.22	3.03	4.88	9.22	50.29	48.54	47.39
FeO_T	0.50	0.54	0.74	12.51	23.23	16.17	83.98	77.53	73.55	38.01	41.54	41.85
MnO	0.00	0.02	0.00	0.40	0.73	0.88	0.33	0.49	0.57	1.47	1.34	1.36
MgO	0.09	0.04	0.03	13.69	19.98	26.33	0.62	0.99	1.37	4.70	5.20	4.89
CaO	7.22	9.90	8.45	18.27	3.52	1.15	0.21	0.11	0.05	0.49	0.15	0.16
Na_2O	7.39	5.12	6.36	0.32	0.10	0.00	0.01	0.02	0.00	0.02	0.00	0.00
K_2O	0.35	0.30	0.33	0.04	0.00	0.03	0.09	0.02	0.02	0.05	0.00	0.03
Cr_2O_3	0.00	0.01	0.00	0.28	0.01	0.06	2.58	9.06	8.86	0.78	0.78	0.96
V_2O_3	0.01	0.00	0.00	0.03	0.00	0.01	0.05	0.07	0.12	0.38	0.36	0.35
NiO	0.00	0.04	0.00	0.09	0.04	0.10	0.29	0.31	0.28	0.01	0.09	0.00
Total:	99.46	98.75	99.80	98.78	101.72	100.37	93.18	95.50	96.15	97.45	98.39	97.24
FeO							33.20	34.15	37.43	35.93	33.20	32.62
Fe_2O_3							56.44	48.21	40.14	2.30	9.27	10.26
Total:							98.83	100.32	100.17	97.68	99.31	98.27
Proportions of end-members (mol%)												
An	34.4	50.7	41.5									
Ab	63.7	47.4	56.6									
Or	2.0	1.8	2.0									
An%	**35.1**	**51.7**	**42.3**									
Wo				38.8	7.1	2.3						
En				40.5	56.2	72.7						
Fs				20.7	36.7	25.1						
Mg#				**66.1**	**60.5**	**74.4**						
Spl							2.8	4.4	5.1			
Usp							4.7	7.5	14.9			
Chr							4.2	14.5	15.1			
Mag							88.2	73.6	64.9			
Ilm										95.7	84.0	82.2
Hem										4.3	16.0	17.8

Anorthite molar proportion: An% = Ca/(Ca + Na) x 100%. Magnesium number: Mg# = Mg/(Mg + Fe) x 100%. Mineral abbreviations after (*46*).

Table S7. Representative electron microprobe analyses of apatite in clast C27.

Analysis label	pt1	pt3	pt4	pt5	pt6	pt7
			Element oxides (wt%)			
SiO_2	0.22	0.27	0.35	0.25	0.30	0.26
Al_2O_3	0.04	0.03	0.06	0.02	0.02	0.03
TiO_2	0.00	0.01	0.04	0.04	0.02	0.00
FeO_T	0.58	0.70	1.07	0.88	1.53	0.86
MnO	0.14	0.18	0.11	0.04	0.11	0.13
MgO	0.00	0.00	0.00	0.05	0.06	0.01
CaO	53.45	52.87	52.72	53.74	53.53	53.46
Na_2O	0.03	0.08	0.12	0.03	0.00	0.10
K_2O	0.01	0.00	0.03	0.00	0.00	0.00
P_2O_5	39.37	39.44	40.04	40.44	40.13	40.15
PbO	0.03	0.08	0.00	0.00	0.00	0.00
ThO_2	0.05	0.07	0.00	0.02	0.11	0.09
UO_2	0.03	0.00	0.00	0.08	0.00	0.00
SO_3	0.13	0.14	0.07	0.10	0.11	0.13
SrO	0.17	0.00	0.00	0.00	0.08	0.12
Y_2O_3	0.08	0.00	0.02	0.10	0.05	0.07
La_2O_3	0.05	0.00	0.02	0.04	0.08	0.00
Ce_2O_3	0.02	0.07	0.08	0.01	0.12	0.11
Nd_2O_3	0.11	0.05	0.08	0.00	0.00	0.04
F	1.12	0.83	0.59	1.75	1.84	0.69
Cl	4.16	4.48	4.93	3.34	2.84	4.48
Total:	98.38	97.92	98.96	99.43	99.51	99.43
			Proportions of end-members (mol%)			
F	31.1	23.2	16.4	47.6	50.3	18.9
Cl	62.1	67.0	73.1	48.9	41.7	66.1
OH	6.8	9.8	10.5	3.5	8.0	15.0

The proportion of OH is calculated based on the assumption that F + Cl + OH = 1 per 13 oxygens.

Table S8. Chondrite-normalized Rare Earth Elements concentration of selected zircons from NWA 7533 as well as the 91500 terrestrial zircon standard. Chondrite normalization parameter are from (*47*).

REEs	S24B4	S24B7	S25B11	S23B16	S25B10	S25B12	S25B14	91500-1	91500-2	91500-3
La	0.83	0.28	1.73	2.13	1.01	2.09	1.44	0.52	0.43	0.47
Ce	2.94	2.07	2.59	5.47	2.68	5.25	2.23	4.42	4.04	4.33
Pr	1.77	0.70	1.77	1.82	1.87	2.12	2.04	0.81	0.66	0.71
Nd	4.99	2.37	5.00	2.49	5.51	3.64	4.64	0.96	0.85	0.91
Sm	25.44	12.00	25.22	8.63	29.43	15.66	21.52	2.89	2.57	2.93
Eu	16.66	8.30	18.63	4.34	18.53	11.58	6.42	4.16	3.66	3.91
Gd	116.49	61.88	115.98	48.56	132.29	78.92	98.13	7.87	6.85	7.35
Tb	266.34	149.80	263.54	136.95	299.73	191.61	238.88	19.19	16.46	17.88
Dy	393.00	226.38	379.46	225.72	425.62	287.87	357.59	30.69	29.01	31.07
Ho	615.38	361.06	581.05	393.11	653.54	459.87	581.45	66.72	58.21	61.91
Er	997.22	617.12	949.98	703.21	1057.73	763.84	983.51	112.98	97.89	107.30
Tm	1210.02	779.87	1145.41	900.09	1273.33	932.05	1282.58	192.35	172.28	181.73
Yb	1457.76	1011.46	1352.00	1183.57	1484.88	1132.32	1625.36	384.27	335.84	374.19
Lu	1614.07	1098.99	1504.25	1137.71	1643.67	1228.89	1845.86	407.13	379.81	403.19

Table S9. Model melt compositions at different fractionation steps. F is the fraction of the initial melt remaining after each step.

Stage	F	SiO_2	$Al2O_3$	CaO	MgO	FeO	K_2O	Na_2O	TiO_2	Cr_2O_3	Sum
0	1.00	47.82	7.00	5.35	16.65	20.51	0.16	1.42	0.34	0.75	100.00
1	0.90	48.73	7.75	5.91	13.86	20.80	0.18	1.57	0.37	0.83	100.00
2	0.89	49.97	8.70	6.62	10.74	20.65	0.20	1.76	0.42	0.93	100.00
3	0.88	52.33	9.88	7.58	7.65	19.58	0.23	2.02	0.48	0.24	100.00
4	0.86	55.41	11.42	8.81	4.56	16.50	0.27	2.37	0.57	0.09	100.00
5	0.83	57.65	10.07	8.85	3.64	16.26	0.32	2.48	0.67	0.08	100.00
6	0.80	59.26	9.34	8.29	2.75	16.66	0.38	2.56	0.71	0.04	100.00
7	0.75	61.94	8.45	7.59	1.93	16.68	0.47	2.51	0.43	0.02	100.00
8	0.67	66.81	7.16	6.69	1.09	15.16	0.60	2.18	0.29	0.00	100.00
9	0.50	76.67	5.50	5.00	0.44	9.76	0.89	1.58	0.16	0.00	100.00
10	0.00	76.87	7.09	4.10	0.19	7.40	3.12	1.15	0.08	0.00	100.00

Table S10. Model compositions of liquid and solid phases at different fractionation steps. F is the fraction of different phases. Mineral abbreviations after (*46*).

Stage	Phase	F	T	SiO_2	Al_2O_3	CaO	MgO	FeO_t	K_2O	Na_2O	TiO_2	Cr_2O_3	SUM	*X*
0	Liq	1.000	1519	47.030	4.057	5.640	24.411	16.869	0.100	1.352	0.250	0.290	100.0	0.59
1	Liq	0.900	1458	48.761	4.570	6.341	20.679	17.405	0.113	1.523	0.282	0.327	100.0	0.54
1	Ol	0.100	1458	33.333	0.000	0.090	53.949	12.627	0.000	0.000	0.000	0.000	100.0	0.81
2	Liq	0.889	1376	50.992	5.230	7.241	16.344	17.623	0.129	1.743	0.323	0.375	100.0	0.48
2	Ol	0.111	1376	33.333	0.000	0.117	50.654	15.896	0.000	0.000	0.000	0.000	100.0	0.76
3	Liq	0.875	1272	54.164	6.028	8.406	11.801	16.949	0.150	2.030	0.375	0.096	100.0	0.41
3	Ol	0.116	1272	33.333	0.000	0.165	45.609	20.893	0.000	0.000	0.000	0.000	100.0	0.69
3	Spn	0.009	1272	0.000	7.734	0.000	12.275	37.772	0.000	0.000	0.095	42.125	100.0	0.84
4	Liq	0.857	1117	58.260	7.076	9.924	7.143	14.511	0.180	2.419	0.449	0.038	100.0	0.33
4	Pl	0.005	1117	55.658	22.171	19.342	0.000	0.000	0.014	2.815	0.000	0.000	100.0	0.93
4	Ol	0.135	1117	33.333	0.000	0.262	36.520	29.885	0.000	0.000	0.000	0.000	100.0	0.55
4	Spn	0.002	1117	0.000	14.634	0.000	8.774	41.393	0.000	0.000	0.334	34.865	100.0	0.70
5	Liq	0.833	1086	60.543	6.233	9.955	5.700	14.276	0.214	2.521	0.526	0.032	100.0	0.29
5	Pl	0.100	1086	57.210	21.395	17.790	0.000	0.000	0.020	3.585	0.000	0.000	100.0	0.91
5	Ol	0.056	1086	33.333	0.000	0.331	31.317	35.018	0.000	0.000	0.000	0.000	100.0	0.47
5	Pig	0.010	1086	49.207	1.170	4.830	23.493	19.741	0.043	0.479	0.945	0.091	100.0	0.54
5	Spn	0.000	1086	0.000	10.742	0.000	6.242	44.069	0.000	0.000	0.622	38.326	100.0	0.78
6	Liq	0.800	1063	62.411	5.797	9.351	4.317	14.669	0.254	2.617	0.565	0.018	100.0	0.23
6	Pl	0.085	1063	59.459	20.271	15.541	0.000	0.000	0.033	4.697	0.000	0.000	100.0	0.87
6	Ol	0.003	1063	33.333	0.000	0.370	24.402	41.895	0.000	0.000	0.000	0.000	100.0	0.37
6	Cpx	0.062	1063	50.345	0.785	14.790	15.974	16.753	0.072	0.724	0.356	0.201	100.0	0.49
6	Pig	0.050	1063	49.607	0.976	5.810	19.200	22.718	0.063	0.636	0.919	0.070	100.0	0.46
7	Liq	0.750	1039	65.252	5.244	8.564	3.028	14.690	0.313	2.561	0.341	0.007	100.0	0.17

7	Pl	0.108	1039	62.464	18.768	12.536	0.000	0.000	0.060	6.172	0.000	0.000	100.0	0.80
7	Cpx	0.104	1039	50.547	0.674	12.921	13.033	21.442	0.097	0.790	0.399	0.095	100.0	0.38
7	Pig	0.034	1039	50.202	0.694	7.245	14.531	25.784	0.091	0.737	0.670	0.046	100.0	0.36
7	Ilm	0.004	1039	0.000	0.000	0.000	0.000	50.000	0.000	0.000	50.000	0.000	100.0	–
8	Liq	0.667	1003	70.152	4.430	7.530	1.713	13.314	0.404	2.222	0.232	0.002	100.0	0.11
8	Pl	0.142	1003	64.923	17.538	10.077	0.000	0.000	0.112	7.349	0.000	0.000	100.0	0.73
8	Cpx	0.189	1003	50.658	0.604	10.970	8.937	27.341	0.147	0.827	0.487	0.029	100.0	0.25
8	Ilm	0.001	1003	0.000	0.000	0.000	0.000	50.000	0.000	0.000	50.000	0.000	100.0	–
9	Liq	0.500	924	79.619	3.364	5.557	0.675	8.476	0.593	1.590	0.127	0.000	100.0	0.07
9	Pl	0.174	924	66.117	16.941	8.883	0.000	0.000	0.210	7.848	0.000	0.000	100.0	0.69
9	Cpx	0.264	924	50.807	0.603	11.591	4.655	30.769	0.273	0.799	0.497	0.006	100.0	0.13
9	Ilm	0.000	924	0.000	0.000	0.000	0.000	50.000	0.000	0.000	50.000	0.000	100.0	–
9	Q	0.062	924	100.000	0.000	0.000	0.000	0.000	0.000	0.000	0.000	0.000	100.0	–
10	Liq	0.000	889	80.848	4.394	4.623	0.298	6.505	2.094	1.173	0.065	0.000	100.0	0.04
10	Pl	0.215	889	68.228	15.886	6.772	0.000	0.000	1.647	7.467	0.000	0.000	100.0	0.60
10	Cpx	0.256	889	51.236	1.026	14.543	2.309	28.996	0.941	0.514	0.434	0.001	100.0	0.07
10	Q	0.529	889	100.000	0.000	0.000	0.000	0.000	0.000	0.000	0.000	0.000	100.0	–

Dataset S1. (separate file)

U-Pb data and description of zircon and baddeleyite crystals investigated by solution mode analyses.

SI References

1. L. C. Bouvier *et al.* Evidence for extremely rapid magma ocean crystallization and crust formation on Mars. *Nature* **558**, 586–589 (2018).

2. D. J. Condon, B. Schoene, N. M. McLean, S. A. Bowring, R. R. Parrish. Metrology and traceability of U–Pb isotope dilution geochronology (EARTHTIME Tracer Calibration Part I). *Geochim. Cosmochim. Acta* **164**, 464–480 (2015).

3. T. E. Krogh (1973) A low contamination method for hydrothermal decomposition of zircon and extraction of U and Pb for isotopic age determination. *Geochim. Cosmochim. Acta* **37**, 485–494 (1973).

4. F. Corfu. U–Pb age, setting and tectonic significance of the anorthosite–mangerite–charnockite–granite suite, Lofoten-Vesterålen, Norway. *J. Petrol.* **56**, 2081–2097 (2004).

5. H. Gerstenberger, G. Haase. A highly effective emitter substance for mass spectrometric Pb isotope ratio determinations. *Chem. Geol.* **136**, 309–312 (1997).

6. A. H. Jaffey, K. F. Flynn, L. E. Glendenin, W. C. Bentley, A. M. Essling. Precision measurement of half-lives and specific of ^{235}U and ^{238}U. *Phys. Rev.* **C4**, 1889–1906 (1971).

7. R.H. Steiger, E. Jager. Subcommission on geochronology: Convention on the use of decay constants in geo- and cosmochronology. *Earth Planet. Sci. Lett.* **36**, 359–362 (1977).

8. M. Bizzarro, J. A. Baker, D. Ulfbeck. A new digestion and chemical separation technique for rapid and highly reproducible of Lu/Hf and Hf isotope ratio in geological material by MC-ICP-MS. *Geostandard Newslett.* **27**, 133–145 (2003).

9. J. N. Connelly, D. G. Ulfbeck, K. Thrane, M, Bizzarro, T. Housh. A method for purifying Lu and Hf for analysis by MC-ICP-MS using TODGA resin. *Chem. Geol.* **233**, 126–136 (2006).

10. C. Paton, J. Hellstrom, B. Paul, J. Woodhead, J. Hergt. Iolite: freeware for the visualisation and processing of mass spectrometric data. *J. Anal. At. Spectrom.* **26** 2508–2518 (2011).

11. M. Wiedenbeck, P. Allé, F. Corfu, W. L. Griffin, M. Meier, F. Oberli, A. von Quadt, J. C. Roddick, W. Spiegel. Three natural zircon standards for U-Th-Pb, Lu-Hf, trace element and REE analyses. *Geostandard Newslett* **19**, 1–23 (1995).

12. J. Blichert-Toft. Hf isotopic composition of zircon reference material 91500. *Chem. Geol.* **253**, 252-257 (2008).

13. U. Söderlund, P. J. Patchett, J. D. Vervoort, C. E. Isachsen. The ^{176}Lu decay constant determined by Lu-Hf and U-Pb isotope systematics of Precambrian mafic intrusions. *Earth Planet. Sci. Lett.* **219**, 311–324 (2004).

14. A. Bouvier, J. D. Vervoort, P. J. Patchett. The Lu–Hf and Sm–Nd isotopic composition of CHUR: constraints from unequilibrated chondrites and implications for the bulk composition of terrestrial planets. *Earth Planet. Sci. Lett.* **273**, 48–57 (2008).

15. M. Wiedenbeck *et al.* Further characterisation of the 91500 zircon crystal. *Geostand. Geoanalytical Res.* **28**, 9–39 (2004).

16. I. S. E. Carmichael, The iron-titanium oxides of salic volcanic rocks and their associated ferromagnesian silicates. *Contrib. Mineral. Petrol.* **14**, 36–64 (1967).

17. M. J. Whitehouse, B. Kamber. Assigning dates to thin gneissic veins in high-grade metamorphic terranes: A cautionary tale from Akilia, Southwest Greenland. *J. Petrol.* **46**, 291–318 (2005).

18. M. Schuhmacher, E. de Chambost, K. D. McKeegan, T. M. Harrison, H. N. Migeon. In situ U/Pb dating of zircon with the CAMECA ims 1270. In Secondary Ion Mass Spectrometry SIMS IX. Benninghoven A, Nihei Y, Shimizu R, Werner HW (eds) John Wiley, Chichester, UK, pp 919–922 (1993)

19. M. Wiedenbeck *et al.* Three natural zircon standards for U-Th-Pb, Lu-Hf, trace element and REE analyses. *Geostandard Newslett.* **19**, 1–23 (1995).

20. J. S. Stacey, J. D. Kramers. Approximation of terrestrial lead isotope evolution by a two-stage model. *Earth Planet. Sci. Lett.* **26**, 207–221 (1975).

21. L. Nasdala *et al.* Zircon M257 - a homogeneous natural reference material for the ion microprobe U-Pb analysis of zircon. *Geostand. Geoanalytical Res.* **32**, 247–265 (2008).

22. R. A. Stern, S. Bodorkos, S. L. Kamo, A. H. Hickman, F. Corfu. Measurement of SIMS instrumental mass fractionation of Pb isotopes during zircon dating. *Geostand. Geoanalytical Res.* **33**, 145–168 (2009).

23. R. B. Ickert. Algorithms for estimating uncertainties in initial radiogenic isotope ratios and model ages. *Chem. Geol.* **340**, 131–138 (2013).

24. M. Sayab *et al.* Three-dimensional textural and quantitative analyses of orogenic gold at the nanoscale, *Geology* **44**, 739–742 (2016).

25. J.-P. Suuronen, M. Sayab, 3D nanopetrography and chemical imaging of datable zircons by synchrotron multimodal X-ray tomography, *Sci. Rep.* **8**, 4747 (2018).

26. W. Liu, G. E. Ice, X-ray Laue Diffraction Microscopy in 3D at the Advanced Photon Source. In: R. Barabash & G.E. Ice (eds.), *Strain and Gradients from Diffraction*, Imperial College Press (2014).

27. A. R. Santos *et al.* Petrology of igneous clasts in Northwest Africa 7034: Implications for the petrologic diversity of the Martian crust. *Geochim. Cosmochim. Acta* **157**, 56–85 (2015).

28. R. H. Hewins *et al.* Regolith breccia Northwest Africa 7533: Mineralogy and petrology with implications for early Mars. *Meteorit. Planet. Sci.* **52**, 89–124 (2017).

29. F. M. McCubbin *et al.* Geologic history of Martian regolith breccia Northwest Africa 7034: Evidence for hydrothermal activity and lithologic diversity in the Martian crust. *J. Geophys. Res. Planets* **121**, 2120–2149 (2016).

30. S. Hu *et al.* Ancient geologic events on Mars revealed by zircons and apatites from the Martian regolith breccia NWA 7034. *Meteorit. Planet. Sci.* **54**, 850–879 (2019).

31. A. Nemchin *et al.* Record of the ancient Martian hydrosphere and atmosphere preserved in zircon from a Martian meteorite. *Nature Geosci.* **7**, 638–642 (2014).

32. J. J. Belluci *et al.* Pb-isotopic evidence for an early, enriched crust on Mars. *Earth Planet. Sci. Lett.* **410**, 34–41 (2015).

33. W. S. Cassata *et al.* Chronology of Martian breccia NWA 7034 and the formation of the Martian crustal dichotomy. *Sci. Adv.* **4**, eaap8306 (2018).

34. G. Dreibus, H. Wänker. Accretion of the Earth and the inner planets. Proceedings of the 27th International Geological Congress, pp. 1–20 (1985).

35. M. Collinet, E. Médard, B. Charlier, J. Vander Auwera, T. L. Grove. Melting of the primitive Martian mantle at 0.5–2.2 GPa and the origin of basalts and alkaline rocks on Mars. *Earth Planet. Sci. Lett.* **427**, 83–94 (2015).

36. R. Powell, T. Holland. An internally consistent dataset with uncertainties and correlations: 3. Applications to geobarometry, worked examples and a computer program. *J. Met. Geol.* **6**, 173–204 (1988).

37. T. J. Holland, E. C. Green, R. Powell. Melting of peridotites through to granites: a simple thermodynamic model in the system KNCFMASHTOCr. *J. Pet.* **59**, 881–900 (2018).

38. E. S. Jennings, T. J. Holland. A simple thermodynamic model for melting of peridotite in the system NCFMASOCr. *J. Pet.* **56**, 869–892 (2015).

39. T. Shao, Y. Xia, X Ding, Y. Cai, M. Song. Zircon saturation in terrestrial basaltic melts and its geological implications. *Solid Earth Sciences* **4**, 27–42 (2019).

40. J. Blichert-Toft, J. D. Gleason, P. Télouk. The Lu–Hf isotope geochemistry of shergottites and the evolution of the Martian mantle–crust system. *Earth Planet. Sci. Lett.* **173**, 25-39 (1999).

41. V. Debaille, Q. Z. Yin, A. D. Brandon, B Jacobsen. Martian mantle mineralogy investigated by the ^{176}Lu–^{176}Hf and ^{147}Sm–^{143}Nd systematics of shergottites. *Earth Planet. Sci. Lett.* **269**, 186–199 (2008).

42. V. Debaille, A. D. Brandon, C. O'Neill, Q. Z. Yin, B. Jacobsen. Early Martian mantle overturn inferred from isotopic composition of nakhlite meteorites. *Nat. Geosci.* **2**, 548–552 (2009).

43. J. T. Shafer *et al.* Trace element systematics and ^{147}Sm–^{143}Nd and ^{176}Lu–^{176}Hf ages of Larkman Nunatak 06319: closed-system fractional crystallization of an enriched shergottite magma. *Geochim. Cosmochim. Acta* **74**, 7307–7328 (2010).

44. T. J. Lapen *et al.* Two billion years of magmatism recorded from a single Mars meteorite ejection site. *Sci. Adv.* **3**, e1600922 (2017).

45. T. J. Lapen *et al.* A younger age for ALH84001 and its geochemical link to shergottite sources in Mars. *Science* **328**, 347–351 (2010).

46. R. Kretz. Symbols for rock-forming minerals. *Am. Min.* **68**, 277–279 (1983).

47. J.-A. Barrat *et al.* Geochemistry of CI chondrites: Major and trace elements, and Cu and Zn Isotopes. *Geochimica et Cosmochimica Acta* **83**, 79–92 (2012).